

Direct numerical simulations of ripples in an oscillatory flow

MARCO MAZZUOLI¹, AMAN G. KIDANEMARIAM^{*2}, and MARKUS UHLMANN²

¹*Department of Civil, Chemical and Environmental Engineering (DICCA), University of Genoa, Via Montallegro 1, 16145 Genova, Italy*

²*Institute for Hydromechanics, Karlsruhe Institute of Technology, 76131 Karlsruhe, Germany*

October 2018

Abstract

Sea ripples are small-scale bedforms which originate from the interaction of an oscillatory flow with an erodible sand bed. The phenomenon of sea ripple formation is investigated by means of direct numerical simulation in which the sediment bed is represented by a large number of fully-resolved spherical grains (i.e, the flow around each individual particle is accounted for). Two sets of parameter values (differing in the amplitude and frequency of fluid oscillations, among other quantities) are adopted which are motivated by laboratory experiments on the formation of laminar rolling-grain ripples. The knowledge on the origin of ripples is presently enriched by insights and by providing fluid- and sediment-related quantities that are difficult to obtain in the laboratory (e.g. particle forces, statistics of particle motion, bed shear stress). In particular, detailed analysis of flow and sediment bed evolution has confirmed that ripple wavelength is determined by the action of steady recirculating cells which tend to accumulate sediment grains into ripple crests. The ripple amplitude is observed to grow exponentially consistent with established linear stability analysis theories. Particles at the bed surface exhibit two kinds of motion depending on their position with respect to the recirculating cells: particles at ripple crests are significantly faster and show larger excursions than those lying on ripple troughs. In analogy with segregation phenomenon of polydisperse sediments the non-uniform distribution of the velocity field promotes the formation of ripples. The wider the gap between the excursion of fast and slow particles, the larger the resulting growth rate of ripples. Finally, it is revealed that, in the absence of turbulence, the sediment flow rate is driven by both the bed shear stress and the wave-induced pressure gradient, the dominance of each depending on the phase of the oscillation period. In phases of maximum bed shear stress, the sediment flow rate correlates more with the Shields number while the pressure gradient tends to drive sediment bed motion during phases of minimum bed shear stress.

^{*}*Current address:* Federal Waterways Engineering and Research Institute (BAW), Karlsruhe, Germany

1 Introduction

Sedimentary patterns in maritime environments are typically caused by different morphogenetic phenomena and can exhibit a wide range of spatial scales varying from a few centimetres to hundreds of meters. The capability to predict the evolution of large-scale bedforms is necessary, for example, to guarantee the durability of marine structures and infrastructures as well as the equilibrium of sensitive benthic ecosystems, thereby preventing extraordinary catastrophic events. Nonetheless, the contextual presence of smaller bedforms cannot be neglected since morphogenetic processes occurring at different scales are not reciprocally independent. It is well known that small-scale bedforms, like ripples, modify the structure of the flow in the vicinity of the bed and they can significantly enhance the transport of sediments and contaminants near the bed (e.g. [Thibodeaux and Boyle, 1987](#)). It has also been shown that model predictions of the sediment flux due to the flow induced by wind waves on a plane bed can be affected by errors that easily exceed 100% of the actual measurements because turbulence diffusion models currently available are not able to describe the turbulent convective events which characterise an oscillatory flow during the flow reversal ([Davies et al., 1997](#)). Such discrepancies are enhanced by the presence of ripples which can significantly amplify the amount of sediment set into suspension.

Sea ripples originate from the action of the flow induced by wind waves on a movable bed under certain flow and sediment conditions. For the sake of simplicity, let us consider the case of monochromatic wind waves developing over a plane bed of cohesionless sediments. Assuming that the linear Stokes wave theory can be used to approximate the irrotational flow far from the bottom, close to the bed the flow turns, at the leading order of approximation, into the oscillatory boundary layer (OBL) generated by harmonic oscillations of pressure gradient. In real ocean, additional streaming (boundary layer streaming) has its origin in the existence of vertical velocities close to the bed originated by the non-uniformity of the flow beneath free-surface waves. Such streaming, which may also play a role on morphogenetic processes, is presently not considered. Mathematically, the flow can be described by the incompressible Navier-Stokes equations defined in a domain bounded by the bed surface. If the bed is fixed, the hydrodynamic problem is globally stable for moderate values of the Reynolds number as long as the fluctuations generated by the bed roughness do not amplify and turbulence appears. However, the material of coastal shelves often consist of cohesionless fine- and medium-sand which can be easily set into motion by waves even for relatively small values of the Reynolds number. For a laminar OBL, when treating the sediment as a continuum, the stability problem can be tackled analytically. The resulting problem is globally unstable, thus we can expect that the amplitude of a small perturbation of the bed surface grows as the critical condition of sediment motion is reached.

See ripples are caused by the instability of the bed surface under the action of flow oscillations and consist in a two-dimensional waviness of the bed surface, the third dimension being orthogonal to flow oscillations, with wavelength ranging from a few (rolling-grain ripples) to some tens of centimetres (vortex ripples), even though three-dimensional patterns have also been observed (e.g. brick-pattern ripples, [Vittori and Blondeaux, 1992](#); [Pedocchi and García, 2009](#)). The mechanism underlying the formation of a bottom waviness in a laminar OBL over a cohesionless plane bed has been fairly well understood since [Sleath \(1976\)](#) observed that the interactions of a small bottom waviness (of infinitesimal amplitude) with the oscillatory flow induces a secondary steady flow, i.e. a steady streaming superimposed on the principal flow oscillations, consisting of two-dimensional recirculating cells. If the steady streaming is strong enough to affect the

motion of sediment particles, sediments tend to pile up where the streamlines of adjacent recirculating cells converge and to be eroded elsewhere. The mechanism of accumulation of sediments is balanced by the effect of gravitational acceleration which opposes the accretion of the waviness amplitude. Rolling-grain ripples are the bedforms that can form in a laminar OBL and their emergence is the first indicator that a plane bed configuration is evolving into rippled geometry. Experimentally, it was observed that, since their first appearance, ripples undergo a coarsening process that can stop if a stable configuration is attained, when the effect of gravity on sediment particles counteracts that of the steady streaming, before the ripple steepness, defined as the ratio between ripple height and wavelength, causes flow separation (Stegner and Wesfreid, 1999; Rousseaux et al., 2004). As the slope of rolling-grain ripples becomes large enough to trigger the separation of the flow from their crests, vortex ripples form which are characterized by steeper slopes and larger height and wavelength than rolling-grain ripples.

As long as the boundary layer does not separate from the bed surface, the growth rate of wavy bedforms may be determined through linear stability analysis. This approach was first adopted by Lyne (1971) and Sleath (1976) under the hypothesis of large fluid displacement oscillations, i.e. much larger than the wavelength of the bedforms, which however is not suitable for the case of ripples. Then, Blondeaux (1990) solved the analytic problem for arbitrary ratios of the orbital excursion to the ripple wavelength while Vittori and Blondeaux (1990) extended the formulation of Blondeaux (1990) to the case of finite amplitude ripples by means of weakly-nonlinear stability analysis. Laboratory experiments (e.g. Blondeaux et al., 1988) show that stable rolling-grain ripples can be observed only for a relatively small range of values of the Stokes and particle Reynolds numbers and of the mobility number defined, respectively, by:

$$Re_\delta = \frac{U_0^* \delta^*}{\nu^*} \quad , \quad Re_d = \frac{U_0^* d^*}{\nu^*} \quad \text{and} \quad \psi = \frac{U_0^{*2}}{v_s^{*2}} \quad , \quad (1)$$

where U_0^* denotes the amplitude of free-stream velocity oscillations, $\delta^* = \sqrt{2\nu^*/\omega^*}$ denotes the conventional thickness of a viscous oscillatory boundary layer (Sleath, 1984) and ω^* the angular frequency of flow oscillations. The quantity v_s^* is often referred to as *gravitational velocity* of sediment particles and is defined as

$$v_s^* = \sqrt{\left(\frac{\varrho_s^*}{\varrho^*} - 1\right) g^* d^*} \quad (2)$$

where g^* indicates the modulus of gravitational acceleration, ϱ_s^* and d^* the density and the nominal diameter of sediment grains while ϱ^* and ν^* are the density and the kinematic viscosity of the fluid. The period of the flow oscillations is denoted by T^* and equal to π/ω^* . The star superscript is used to denote dimensional quantities and distinguish them from dimensionless ones. The parameters (1), along with the specific gravity $s = \varrho_s^*/\varrho^*$, can be chosen to determine the parameter space for sediment transport with spherical particles in the absence of bedforms. Alternatively, the Galilei number Ga is often used in the particulate flow and suspension communities, which is related to ψ and Re_d through the expression $Ga = Re_d/\sqrt{\psi}$, as well as the Keulegan-Carpenter number, $K_c = Re_\delta^2/(2 Re_d)$, that is defined as the ratio between the semi-excursion of the fluid far from the bed, $\ell_f^* = U_0^*/\omega^*$, and the diameter of sediment particles. As the *average ripple steepness* exceeds the threshold 0.1 identified empirically by Sleath (1984), the flow separates from the ripple crests and computations of the ripple evolution can only be made numerically. For instance, Scandura et al. (2000) studied numerically

the interaction of an oscillatory flow with a wavy wall, characterized by steepness ~ 0.1 , for values of Re_δ ranging between 42 and 89, and observed the flow separation from the crests of the wall and the appearance of three-dimensional vortex structures. However, [Scandura et al. \(2000\)](#) concluded that movable bed should be considered in the simulations to obtain results relevant for the problem of sediment transport.

Since the evolution of the bed surface is not known a priori but results from the coupling between the fluid and sediment dynamics, a discrete approach seems more suitable to investigate the mechanics of sediment particles in an OBL. In order to investigate the origin of ripples and test the capability of the numerical approach to catch the basic physics of the sediment transport, [Mazzuoli et al. \(2016\)](#) performed Direct Numerical Simulations (DNSs) of an oscillatory flow both over smooth and rough walls with movable spherical beads on top of it. The values of the parameters were chosen similar to those of laboratory experiments where the formation either of sediment patterns ([Hwang et al., 2008](#)) or of rolling-grain ripples ([Blondeaux et al., 1988](#)) had been observed. [Mazzuoli et al. \(2016\)](#) considered identical beads initially aligned along the direction of flow oscillations and observed that, within a few oscillation periods, they rearranged in chains orthogonal to the flow oscillations, equispaced by a distance comparable to that measured in the experiments. Qualitatively, the mechanism of formation of the chains was not very sensitive to the number of beads or the presence of the bottom roughness consisting of beads closely packed and fixed on the bottom. Steady recirculating cells of different sizes initially developed, but only recirculating cells compatible with the wavelength of the chains of beads were promoted and could be observed at the final stages of the simulations.

Since the process of formation of chains of spheres is basically different from that of ripples, due to gravity playing different roles in the two cases, two of the experiments of [Blondeaux et al. \(1988\)](#), where rolling-grain ripples formed, were reproduced by means of DNS and are presently described. The values of the relevant dimensional parameters characterising the experiments are reported in table 1. In particular, the present

	T^* [s]	U_0^* [m/s]	ℓ_f^* [m]	δ^* [mm]	d^* [mm]	ϱ_s^*/ϱ^*
run 1	1.86	0.16	0.8	0.05	0.2 ± 0.06	2.65
run 2	0.95	0.13	0.6	0.02	0.2 ± 0.06	2.65

TABLE 1: Parameters for [Blondeaux et al. \(1988\)](#)’s experiments presently considered. From left to right: the oscillation period, the amplitude of free-stream velocity oscillations, the stroke or fluid semi-excursion, the thickness of the Stokes boundary layer, the particle diameter and the particle specific gravity. The kinematic viscosity of the fluid was approximately equal to 10^{-6} m²/s.

investigation is aimed at: (i) showing that laboratory experiments of the formation of ripples can be reproduced by DNS, (ii) obtaining accurate values of quantities that are difficult to be measured in the laboratory (e.g. particle forces and trajectories, steady streaming intensity, bed shear stress, the sediment flow rate), (iii) investigating the dynamics of sediment particles, and (iv) relating the sediment transport to mean flow quantities.

In the following, the numerical method is briefly described while the results are discussed in §3. Finally, conclusive remarks are drawn in §4.

2 Formulation of the problem and numerical approach

The OBL (over a smooth wall) can be generated in the laboratory by the harmonic motion of a piston which produces a uniform pressure gradient through the fluid, in a duct with sufficient depth and breadth to prevent undesirable boundary effects. Typically the axis of the duct develops along a U-shape profile in order to exploit the support of gravity, while only the flow field in the central section of the U-tube, in the vicinity of the bottom, is investigated. The time-development of the pressure gradient driving the flow is described by

$$\frac{\partial p_f^*}{\partial x_1^*} = -\varrho^* U_0^* \omega^* \sin(\omega^* t^*); \quad \frac{\partial p_f^*}{\partial x_2^*} = 0; \quad \frac{\partial p_f^*}{\partial x_3^*} = 0 \quad (3)$$

where t^* is the time variable and (x_1^*, x_2^*, x_3^*) is a Cartesian coordinate system with origin at the bottom of the domain, the x_1^* -axis parallel to the flow oscillations and the x_2^* -axis pointing the upward wall-normal (i.e. bottom-normal) direction. The total pressure can be expressed by the sum:

$$p_{tot}^*(x_1^*, x_2^*, x_3^*, t^*) = \frac{Re_\delta}{2} p_f^*(t^*) + p^*(x_1^*, x_2^*, x_3^*, t^*), \quad (4)$$

where p_f^* is equal to the right hand side of the first component of (3) multiplied by x_1^* and p^* denotes the pressure in the boundary layer. Then, p^* (as well as any other flow quantity) can be further split into the sum of two contributions:

$$p^*(x_1^*, x_2^*, x_3^*, t^*) = \bar{p}^* + p'^*(x_1^*, x_2^*, x_3^*, t^*), \quad (5)$$

the flat overbar indicating the statistical average operator (the ensemble average or the phase average, i.e. the average computed at corresponding phases of the oscillation period, if the flow and bed evolution are at the equilibrium) and p'^* the corresponding fluctuating part. Let the bottom (i.e. the plane $x_2^* = 0$) be equipped with a bed of monosized spherical heavy particles of diameter d^* initially arranged in multiple superimposed plane layers. The dynamics of the particles is dictated by the collective influence of gravity, collision and hydrodynamic forces. Hydrodynamic force, in turn, results from the combination of pressure and viscous contributions. The pressure gradient (3) drives both the motion of the fluid and of the solid particles while the fluctuations of pressure, denoted by p'^* in equation 5, can be associated both with turbulence and with the motion of particles. Since the ensemble average is not feasible with a single simulation while the “equilibrium state” is presently never attained, different spatial-average operators are adopted to estimate the average quantities. The operator $\langle \cdot \rangle_\alpha^{(i)}$ denotes the average of the argument performed along the direction $\alpha \equiv x_1, x_2$ or x_3 , or along two directions, e.g. $\alpha \equiv x_1 x_3$ indicates the horizontal plane (*plane average*), or over a three-dimensional sub-space $\alpha \equiv \mathcal{V}$ (*volume average*). For the sake of simplicity, omitting α implicitly indicates that the plane average is performed. The superscript (i) , if present, indicates that the flow field has been split into a number of bins either along the streamwise direction, equispaced by $h_1^* = 2d^*$, or along the wall-normal direction, equispaced by $h_2^* = d^*$, and that the average is computed over the i -th bin. A similar notation is adopted for particle-related quantities to indicate the average over a set of particles ($\alpha \equiv s$) or the time-average over each half-period ($\alpha \equiv T/2$).

On the basis of purely dimensional considerations, for the present flow configuration, a generic hydrodynamic quantity \mathcal{F}^* can be expressed as a function $\mathcal{F}^*(x_i^*, t^*; \omega^*, U_0^*, d^*, g^*, \mu^*, \varrho^*, \varrho_s^*)$, $i = 1, 2, 3$, where $\mu^* = \varrho^* \nu^*$ denotes the dynamic viscosity of the fluid. The

	Re_δ	Re_d	ψ	Ga	K_c	s
run 1	128	33.3	9.69	10.7	246	2.46
run 2	71.7	17.4	7.88	6.2	148	2.65

TABLE 2: Summary of flow parameters for the present runs.

run	L_{x_1}	L_{x_2}	L_{x_3}	n_{x_1}	n_{x_2}	n_{x_3}	Δt	t_{fin}	N_s
run 1	53.2	26.6	26.6	2048	1024	1024	$1.96 \cdot 10^{-4}$	41π	257138
run 2	49.1	18.4	24.5	2048	768	1024	$2.62 \cdot 10^{-4}$	58π	223442

TABLE 3: Domain and time discretisation for the present runs. The final time of the simulations is denoted by t_{fin} while N_s is the number of spheres used in each run.

present choice is to use ω^* , ϱ^* and μ^* to reduce the number of dimensionally dependent arguments and obtain the corresponding dimensionless quantity $\mathcal{F}(x_i, t; Re_\delta, Re_d, \psi, s)$ which depends on the numbers introduced in §1. The values of the numbers Re_δ, Re_d, ψ and s for the present simulations are indicated in table 2. Note that the specific gravity between the runs differs by 7% which is not expected to play a significant role. Thus, the incompressible Navier-Stokes equations can be expressed in a dimensionless form by introducing the following variables:

$$\begin{aligned} (x_1, x_2, x_3) &= \frac{(x_1^*, x_2^*, x_3^*)}{\delta^*} ; \quad t = t^* \omega^* ; \\ (u_1, u_2, u_3) &= \frac{(u_1^*, u_2^*, u_3^*)}{U_0^*} ; \quad p = \frac{p^*}{\varrho^* (U_0^*)^2} ; \quad (f_1, f_2, f_3) = \frac{(f_1^*, f_2^*, f_3^*)}{U_0^* \omega^*} . \end{aligned} \quad (6)$$

In (6), u_1^*, u_2^*, u_3^* are the fluid velocity components along the x_1^* -, x_2^* - and x_3^* -directions, respectively, and f_1^*, f_2^*, f_3^* are the components of the body force. Hence, the dimensionless continuity and Navier-Stokes equations read:

$$\frac{\partial u_j}{\partial x_j} = 0 \quad (7)$$

$$\frac{\partial u_i}{\partial t} + \frac{Re_\delta}{2} u_j \frac{\partial u_i}{\partial x_j} = -\frac{Re_\delta}{2} \frac{\partial p}{\partial x_i} + \delta_{i1} \sin(t) + \frac{1}{2} \frac{\partial^2 u_i}{\partial x_k \partial x_k} + f_i \quad (8)$$

where Einstein's convention on the summation is used. It can be noted that the Reynolds number Re_δ is the only dimensionless parameter which is based upon purely hydrodynamic quantities and controls the momentum equation (8), while sediments enter the problem through the boundary conditions. Concerning the simulation of the particle motion, the main dimensionless control parameters are the specific gravity of sediments s , the sphere Reynolds number Re_d and the mobility number ψ that are defined in §1.

The domain where equations (7) and (8) are solved numerically is a cuboid space of dimensions L_{x_1} , L_{x_2} and L_{x_3} in the streamwise, wall-normal and spanwise directions, respectively, which are indicated in table 3. While periodic conditions are applied at the boundaries in the streamwise and spanwise directions, the no-slip condition is forced at the bottom, viz.

$$(u_1, u_2, u_3) = (0, 0, 0) \quad \text{at} \quad x_2 = 0 \quad (9)$$

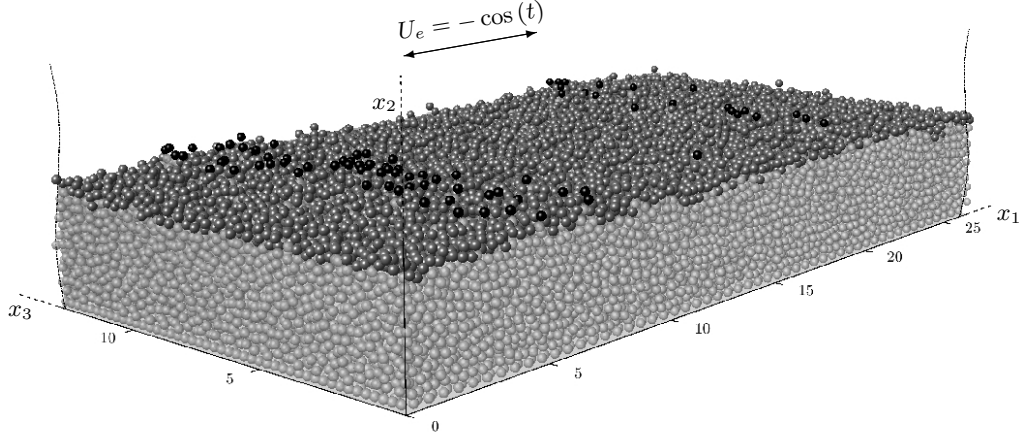


FIGURE 1: Sketch of a simulation (detail of the computational domain). Different colours are used to distinguish *top-layer particles* (dark grey) from *crest particles* (black). Most of the particles shadowed by light grey exhibit negligible displacements with respect to top-layer particles throughout the simulation.

and the free slip condition is forced at the upper boundary:

$$\left(\frac{\partial u_1}{\partial x_2}, \frac{\partial u_3}{\partial x_2} \right) = (0, 0); \quad u_2 = 0 \quad \text{at} \quad x_2 = L_{x_2}. \quad (10)$$

The dimension L_{x_2} of the domain is chosen large enough to guarantee a vanishing shear stress far from the bottom. The choice of the streamwise and spanwise dimensions of the computational domain, L_{x_1} and L_{x_3} , can significantly affect the process of formation of the bedforms. In particular, as recently pointed out by [Kidānemariam and Uhlmann \(2017\)](#), the choice of L_{x_1} allows the development of bedforms characterised by wavelengths equal to $(1, \frac{1}{2}, \frac{1}{3}, \frac{1}{4}, \dots) L_{x_1}$, thus the evolution of the geometrical properties of bedforms are expected to be markedly discontinuous with respect to time. For instance, the larger L_{x_1} the smoother the evolution of bedforms appears. Therefore, the value of L_{x_1} is chosen as large as two times the wavelength of ripples observed in the experiments of [Blondeaux \(1990\)](#) when the “equilibrium state” was reached. Also the value of L_{x_3} is chosen to allow for possible formation of three-dimensional patterns, which were however absent in the experiments. A sketch of the simulations is shown in figure 1.

The hydrodynamic problem is solved throughout the whole computational domain including the space occupied by the solid particles. Indeed, the no-slip boundary condition at the surface of the spheres is forced by means of the (Eulerian) volume force f_1, f_2, f_3 which is simply added to the right hand side of momentum equation (8) via the immersed boundary approach. The flow solver consists of the semi-implicit second-order fractional-step method, based on the finite difference approximation of time- and space-derivatives, as proposed by [Uhlmann \(2005\)](#). The domain is discretised by a uniform equispaced grid of spacing $\Delta x_i^* = d^*/10$ in the i -th direction ($i = 1, 2, 3$). The dynamics of the fluid and solid phases are coupled through the immersed boundary method while collision forces are computed with a soft-sphere Discrete Element Model (DEM) based upon a linear mass-spring-damper system. A detailed description of the collision model and of the validation can be found in [Kidānemariam and Uhlmann \(2014b\)](#). The code has been recently used for different investigations by [Kidānemariam and Uhlmann](#)

(2014a), Uhlmann and Chouippe (2017) and Mazzuoli and Uhlmann (2017) and, in a context similar to the present one, by Mazzuoli et al. (2016).

The start-up bed configuration was obtained by settling approximately 15 layers of spheres (the number of spheres, N_s , used for each run is indicated in table 3) on a flat smooth bottom while the fluid was at rest. One layer of spheres was preliminarily fixed on the bottom with a hexagonal arrangement in order to prevent the whole bed from sliding as a block along the bottom, which was never observed in the laboratory experiments. This expedient did not affect the results of the simulations because the particle velocity rapidly vanishes beneath the surficial layers of particles. The spheres whose centers are located above a distance of $15 d^*$ from the bottom were removed in order to obtain a flat bed surface.

For the first wave-period of each simulation all the particles were kept fixed in order to let the interstitial flow develop. Simulations 1 and 2 were run for 41 and 58 half-cycles, respectively. Hereinafter, “simulation” and “case” can be sometimes used interchangeably in place of “run” referring to runs 1 and 2.

The quantities closely related to the hydrodynamic problem are normalised as in (6), while those more relevant for the evolution of the bed, which are directly affected by the particle dynamics, are preferably shown in terms of particle-related reference quantities (i.e. d^* and v_s^*). Actually, the values of d^*/δ^* for the two simulations are similar (0.26 and 0.24 for runs 1 and 2, respectively), thus the choice of d^* or δ^* as reference length scales is not practically relevant in the present configuration.

3 Results

As mentioned above, the bed was initially leveled in order to start the simulations with a plane-bottom configuration. Let the spheres farthest from the bottom, i.e. whose center is located in the range of one diameter below the farthest one, be hereafter referred to as *crest particles* (cf. black spheres in figure 1). Initially, crest particles are distributed approximately randomly on the bed, as shown by the red spheres in figure 2a. Then, after a few oscillations, crest particles tend to group in short chains or small bunches during half-periods which can eventually be destroyed in the subsequent half-period or merge with each other (see figure 2b). Finally, clear two-dimensional patterns form which then accrete and form the rolling-grain ripples (figure 2c,d). A movie of the formation of ripples for the run 1 can be found online as *supplementary material*.

For the present values of the parameters, only the surficial spheres exhibited significant displacements through rolling motion while no particles were observed saltating or being entrained into suspension. The evolution of the bed surface and the motion of the surficial particles are described in the following.

3.1 Evolution of the bed surface

The bed surface, namely the (fictitious) solid-fluid interface, can be defined on the basis of the sediment volume concentration, hereafter referred to as *particle volume fraction* and denoted by ϕ_s , which is zero far away from the bottom and abruptly increases at the bed. Hence, the bed surface is identified by points where ϕ_s reaches a threshold value. Similarly, in laboratory experiments, the bed-flow interface is often detected by means of an image analysis procedure, thresholding the sideview frames of the bed (e.g. Aussillous et al., 2013). In fact, the b/w intensity of pixels is highly correlated with ϕ_s . This approach was successfully reproduced numerically by Kidanemariam and Uhlmann (2014a) who considered the threshold value $\phi_s = 0.1$. Kidanemariam and Uhlmann

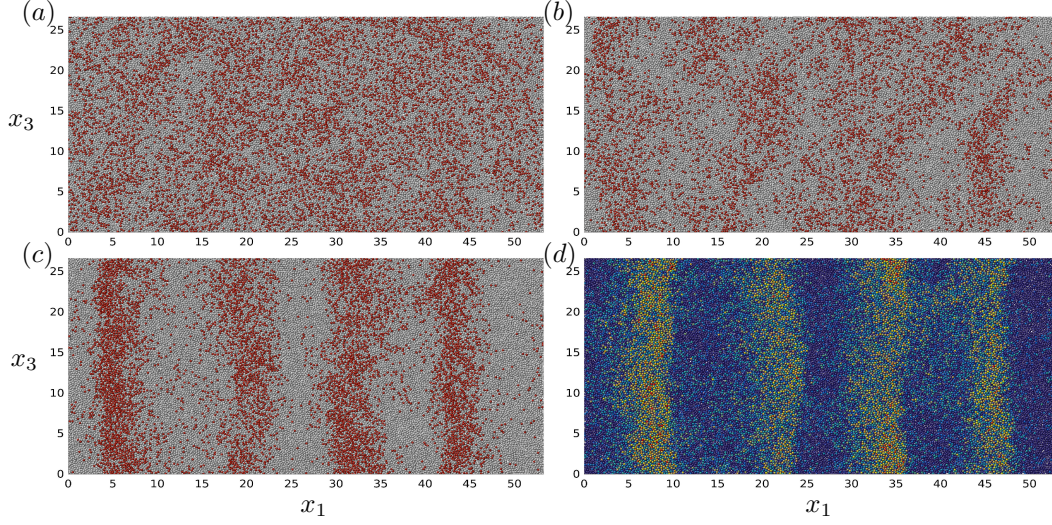


FIGURE 2: Top view of the bed at (a) $t = 7.0$, (b) $t = 44.4$, (c) $t = 137.8$, (d) $t = 142.0$ for run 1. Crest particles are highlighted in red in panels (a – c). In panel (d) particles are highlighted by colours according to their distance from the bottom, increasing from blue to red. The complete time-sequence can be seen in the movie available in the *supplementary material*.

(2014a) defined a sample volume of size $\Delta x_1^* \times \Delta x_2^* \times L_{x_3}^*$ over which the particle volume fraction was evaluated. Therefore, the dependency of ϕ_s on x_3^* was neglected and the *bed profile*, $\eta_\phi^*(x_1^*, t^*)$, was obtained.

Another approach is also presently considered which was first adopted by Mazzuoli et al. (2017) to detect the bed/flow interface. Since spheres are presently not set into suspension, they remain in enduring contact throughout their motion and the bed surface can be thus unambiguously identified by the centers of the spheres on top of others, which are hereafter referred to as *top-layer particles* (cf. dark-grey spheres in figure 1). The i -th sphere ($i = 1, \dots, N_s$) belongs to the top layer if no other sphere centers above the i -th one lie inside the solid angle of magnitude $\Omega = (2 - \sqrt{3})\pi$ sr with respect to the bottom normal. Then, if this condition is fulfilled, the Boolean function \mathcal{E}_i associated with the i -th particle is equal to 1, otherwise it is equal to 0. Therefore, the bed surface is defined as the function interpolating the centers of the spheres characterised by $\mathcal{E} = 1$, and is denoted by $\eta^*(x_1^*, x_3^*, t^*)$. Such definition circumvents the matter of defining a threshold and allows us also to study three-dimensional patterns. Actually, the patterns observed for the present values of the parameters do not show an appreciable dependency on the spanwise coordinate and the bed profile $\eta_\mathcal{E}^*$, defined as equal to $\langle \eta^* \rangle_{x_3}$, is found practically to collapse on η_ϕ^* once it is shifted vertically upward by a constant value $\sim 0.8d^*$ (cf. figure 3). Since the position of the bed profile is analogously detected by the two procedures, henceforth the profile η_ϕ^* is considered.

In the simulations, the average bed elevation $\langle \eta_\phi \rangle_{x_1}$ initially decreases as an effect of the settlement and compaction of the granular bed (not shown here). Then, after a few oscillation periods $\langle \eta_\phi \rangle_{x_1}$ asymptotically reaches a constant value approximately equal to $13.83 d^*$ and $12.12 d^*$ for both runs 1 and 2, respectively, superimposed only by small fluctuations of order $\mathcal{O}(10^{-2}) d^*$, which are related to the different phases of the wave cycle. Correspondingly, the solid volume fraction, ϕ_s , in the region between the bottom and the surface layers of particles does not show significant temporal fluctuations and

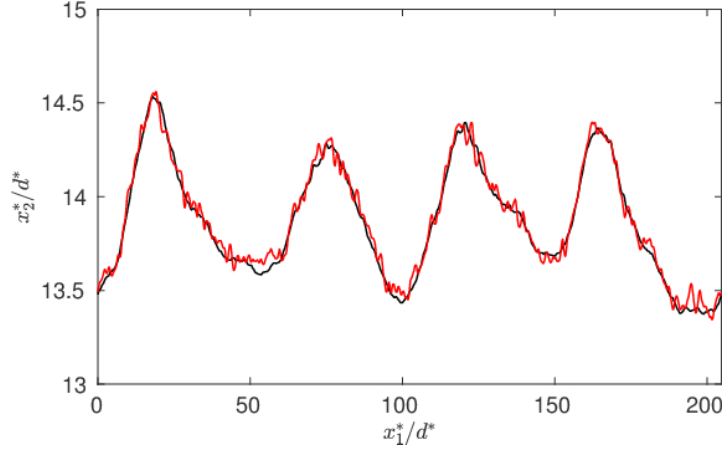


FIGURE 3: Comparison between the bed profiles η_ε (red line) and η_ϕ (black line) at an instant of run no. 1 when rolling-grain ripples are present.

attains the average values 0.49 for both runs. Instead, figure 4 shows the space-time development of the fluctuations of the bed profile about the average bed elevation, i.e. $\eta'_\phi = \eta_\phi - \langle \eta_\phi \rangle_{x_1}$, for runs 1 and 2. While bedforms emerge in the second half of run 1, in run 2 the presence of persistent patterns is difficult to detect by visual inspection of figure 4b. The *root mean square* (rms) of η'_ϕ , η_{rms} , increases with time in both runs (cf. figure 5), whilst the amplitude of the fluctuations attained at the end of run 2 barely reach $0.1 d^*$ (three times smaller than that of run 1). In run 1, the linear regression of $\ln \eta_{rms}$ (red solid line in figure 5a) shows that η_{rms} grows exponentially. Moreover, the regression of relative maxima and minima of η_{rms} computed for each half-period (indicated with dashed lines in figure 5a) preserves the exponent of the mean trend. Thus, the amplification of half-period fluctuations of the bed surface, normalised by the particle diameter, can be approximated by the expression:

$$\mathcal{A}_\eta = (a_{max} - a_{min})e^{bt} \quad (11)$$

where $b = 1.46 \cdot 10^{-2}$ and the factors $a_{max} = 4.98 \cdot 10^{-2}$ and $a_{min} = 3.38 \cdot 10^{-2}$ refer to the average upper and lower bounds of η_{rms} . In other words, the rate of coarsening of ripples is directly proportional to the amplitude of ripples. On the other hand, in run 2, the time development of η_{rms} is not monotonic and the mean growth is slower than that observed for simulation 1 (cf. figure 5b). It is likely that, in a much larger number of oscillation periods, the formation of ripples could be observed more clearly also in case 2, but this would require formidable computational and wall-clock time which are at the moment out of reach.

To detect the wavelength of ripples as a function of time, the bed profile is expanded in Fourier series and the absolute value and the growth rate of each term of the series is investigated. It is evident that the wave numbers $k^* \delta^* = 0.47$ and $k^* \delta^* = 0.25$ dominate the spectra of η'_ϕ at the end of runs 1 and 2, respectively (cf. figure 6). However, since modes are still evolving at the end of each run, an equilibrium condition is not reached and the simulation time is not sufficient to describe the complete evolution of individual modes. Alternatively, the *dominant wavelength* can be defined as two times the space lag, λ_η^* , at which the absolute value of the two-point correlation function of η'_ϕ attains the first maximum value (Kidane-mariam and Uhlmann, 2017). The result of this procedure

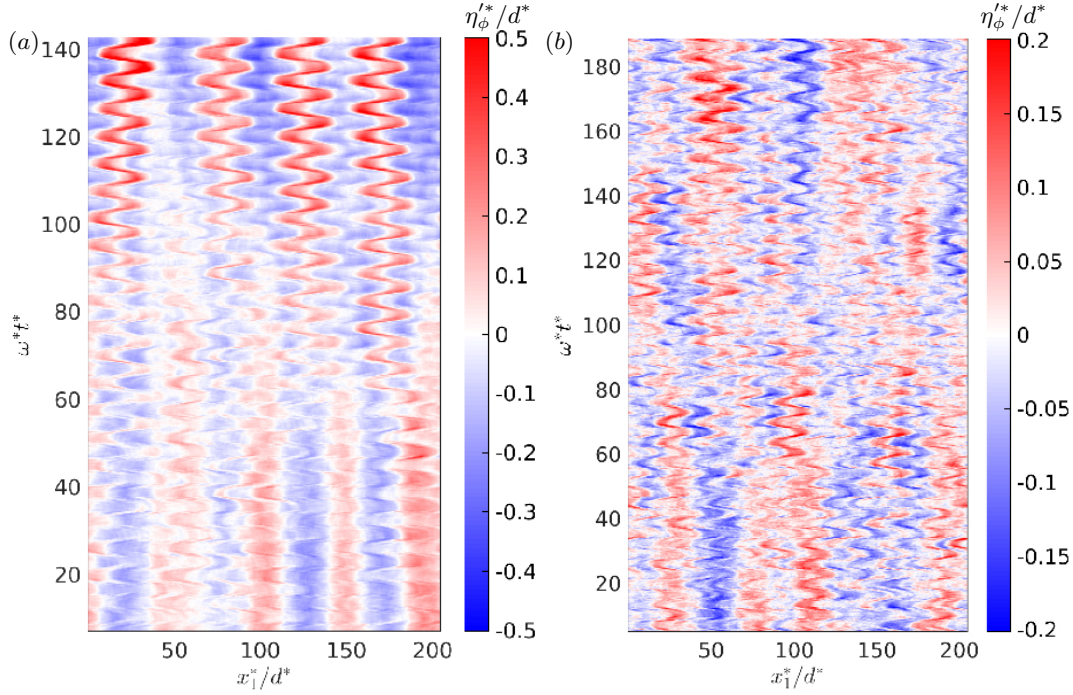


FIGURE 4: Spatio-temporal development of the fluctuations of the bed profile about the average bed elevation, η'_{ϕ}/d^* , for run 1 (a) and run 2 (b).

is shown in figure 7. As predicted by the Fourier analysis, the dominant wavelength for the second half of simulation 1 corresponds to the wave number $k^*\delta^* = 0.47$ ($\lambda_{\eta}^* = 13\delta^*$) while for the last ~ 6 oscillation periods of simulation 2 patterns are characterised by the wave number $k^*\delta^* = 0.25$ ($\lambda_{\eta}^* = 25\delta^*$). The values of λ_{η}^* can be compared with the results of the experiments carried out by Blondeaux et al. (1988) for similar values of the parameters and with those obtained by linear stability analysis by Blondeaux (1990). It is found that the values of λ_{η}^* in the current simulations are comparable to the wavelengths of the first emerging ripples observed in the laboratory. At this stage it is worthwhile to remark on the importance of this result, since a natural very complex phenomenon has been reproduced by a very simplified, though numerically challenging, system, which indicates that the basic process leading to the formation of ripples is somewhat robust. In particular, for the experiment reproduced by run 1, Blondeaux (1990) observed $\lambda_{\eta}^* = 25\delta^*$ ($96 d^*$) while for the case simulated by run 2 the value of λ_{η}^* was approximately equal to $26\delta^*$ ($108 d^*$). Similar results are predicted by means of the linear stability analysis following the approach of Blondeaux (1990) ($\lambda_{\eta}^* = 23\delta^*$ for run 1 and $\lambda_{\eta}^* = 22\delta^*$ for run 2). Rousseaux et al. (2004) carried out experiments also exploring the region of the parameter space where runs 1 and 2 lie and observed the first measured wavelengths $\lambda_{\eta}^* \sim 20 \delta^*$ and $\lambda_{\eta}^* \sim 25 \delta^*$, respectively. Therefore, the wavelength of ripples simulated in run 1 is smaller than the wavelength observed experimentally. Such a discrepancy can be due to several reasons mostly associated with the modelling of particle-particle interactions. The significance of the role of sediment friction in the formation of patterns was emphasised by Moon et al. (2004). Indeed, sand grains can have irregular shape and, consequently, more than one point of contact during a binary collision, which allow

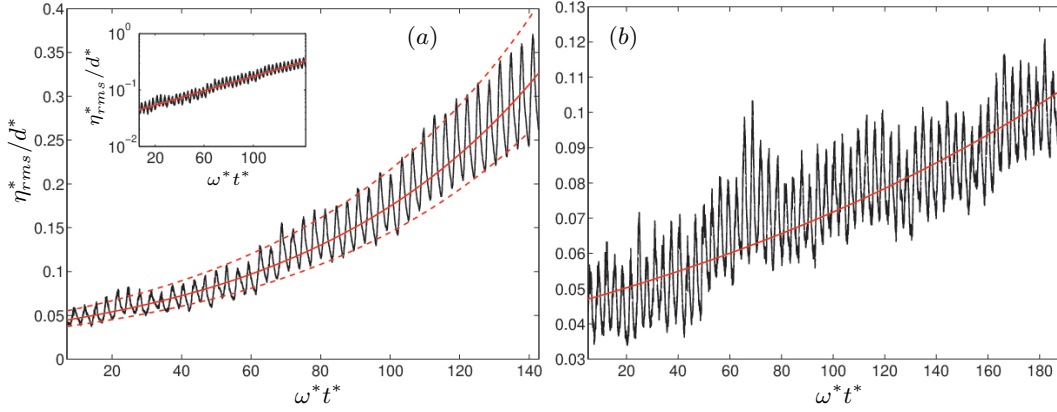


FIGURE 5: The diagrams in panel (a) and (b) show the root mean square of the spatial fluctuations of the bed profile plotted versus time for simulations 1 and 2, respectively. The thick solid (red) lines are the regression curves $a \exp(bt)$, where $a = 0.040$, $b = 1.46 \cdot 10^{-2}$ for run 1 and $a = 0.046$, $b = 4.45 \cdot 10^{-3}$ for run 2. Dashed (red) lines in panel (a) are obtained for $a = a_{min} = 0.034$ and $a = a_{max} = 0.050$. The inset figure in panel (a) highlights the exponential trend of η_{rms} using semi-logarithmic axis scale.

them to transfer linear and angular momentum more efficiently than spheres. Moreover, the sensitivity of sediment dynamics to the contact is enhanced if particles roll over each other (enduring contact) rather than colliding. The particles of run 1 behave like finer sand grains, since, based on the experimental results of Rousseaux et al. (2004), the first measured wavelength tends to increase monotonically with increasing size of sediments and because spherical particles are statistically set into motion more easily and undergo larger excursions than sand grains of irregular shape. On the other hand, figure 6a shows that the modes associated with the wave numbers $k^*\delta^* = 0.35$ and $k^*\delta^* = 0.24$ grow at approximately the same rate as the dominant mode in the last periods of run 1 and it is possible that the four ripples of figure 2 might merge after a certain time.

Even though the ripples of run 1 do not really drift in the streamwise direction, their crests migrate to and fro by several sphere diameters. Therefore, as shown in figure 8, ripple shape changes during the oscillation period. The profiles indicated in figure 8a by (black and red) thick lines are attained in the phases when the fluid far from the bed decelerates and then vanishes (at the flow reversal) while surficial particles are at rest. In these phases, ripples are asymmetric with slopes relatively mild and the lee side steeper than the stoss side (cf. figure 8b). In the subsequent phases, while the flow accelerates, the amplitude of ripples increases, along with their slope, and reaches the maximum value approximately 0.20π earlier than the free-stream velocity does. Now the profile of each ripple is symmetric (thin dashed lines in figure 8a), but then it becomes asymmetric again as the crest proceeds the excursion towards the other side of the ripple. Finally, the opposite resting configuration is attained while the fluid is already decelerating. Hence, most of the bed-profile evolution is carried out during the acceleration phases. At the end of the present simulations the mild (lee) slope of ripples is approximately 0.02 while for the steep (stoss) side the slope ranges between 0.08 and 0.16. Following the empirical approach of Sleath (1984), the flow separation behind the crests should occur if the ratio between the height and the wavelength of ripples, namely the average steepness, reaches the value 0.1. In the period considered in figure 8, the average slope is about 0.02 and the flow does not separate and rolling-grain ripples do not evolve into vortex ripples.

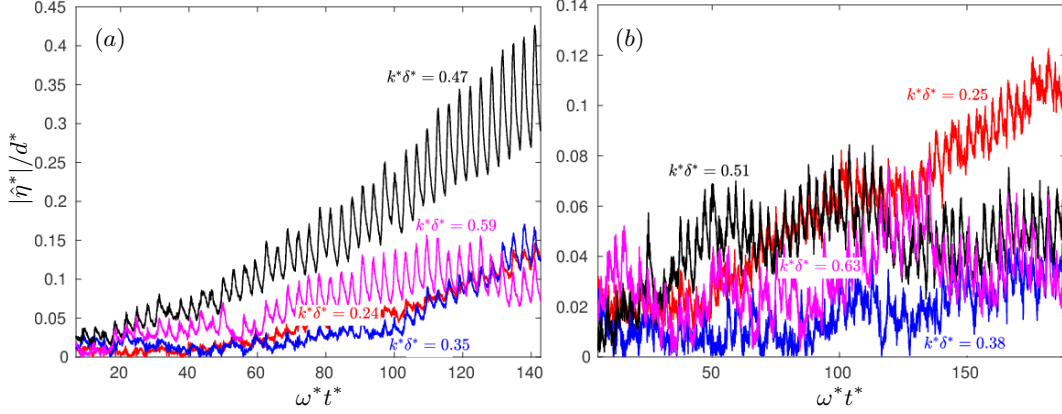


FIGURE 6: Panels (a) and (b) show the absolute value of four Fourier modes of the bed profile plotted versus time for simulations 1 and 2, respectively. Red, blue, black and magenta lines correspond to the 2_{nd} , 3_{rd} , 4_{th} and 5_{th} modes of the bed profile, respectively.

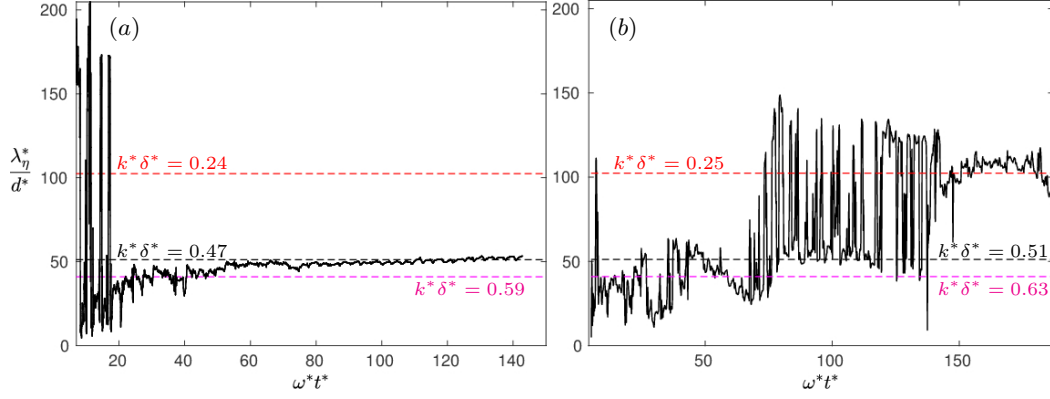


FIGURE 7: Dominant wavelength of the bed profile computed as a function of time for runs 1 (panel (a)) and 2 (panel (b)).

The spectra of the bed profile, $S_{\eta\eta}^*$, are computed as functions of wave numbers at the phases of the oscillation period shown in figure 8 and are plotted in figure 9. Previous research has shown that for wave numbers much smaller than the smallest flow scale which do not affect the stability of the bed and much larger than the grain size, the spectrum was proportional to k^{*-3} (Hino, 1968; Jain and Kennedy, 1974; Nikora et al., 1997; Coleman and Nikora, 2011; Kidanemariam and Uhlmann, 2017). Hino (1968) showed that, when the equilibrium configuration of the bed profile is reached, the spectrum of the bed slope depends linearly on the wave number, whence the exponent -3 for the spectrum of the bed profile is obtained by purely dimensional reasoning. From the geometrical point of view, the -3 power law indicates that the bed profile is self-similar, i.e. the shape of the profile is independent of the length scale (Nikora et al., 1997), in the range of length scales between d^* and λ_{η}^* . Presently, the flow is unsteady and a comparison to bedforms that reached the equilibrium configuration is not possible. However, in the range of wave numbers indicated by Hino (1968), i.e. $0.02 \lesssim k^*d^* \lesssim 0.1$ in figure 9, the spectrum of ripple profiles is observed proportional to k^{*-3} . The same trend can be obtained, in this range of wave numbers, by considering the spectrum of streamwise-periodic ramps (see

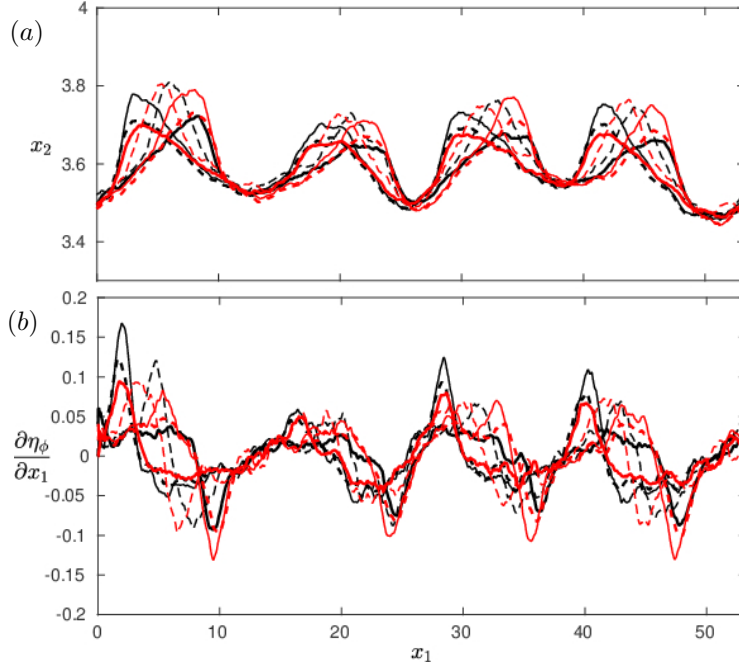


FIGURE 8: Bed profile, η_ϕ , (panel (a)) and bed slope (panel (b)) at different phases of a wave cycle when rolling-grain ripples are formed. Black lines refer to instants $t = 136.7$ (solid, thick), $t = 137.4$ (dashed, thin), $t = 138.2$ (solid, thin) and $t = 139.0$ (dashed, thick) while the mean flow is directed from right to left. Red lines refer to instants $t = 139.8$ (solid, thick), $t = 140.6$ (dashed, thin), $t = 141.4$ (solid, thin), $t = 142.2$ (dashed, thick) during which the mean flow is directed from left to right.

the inset in figure 9). Therefore, the so called “−3 power-law” is associated with the fact the the stoss side of the ripples is mostly straight. In the laboratory or in the field, it is difficult to compute the spectra for large wave numbers because the measurements of the bed surface do not typically reach such high accuracy. For values of k^*d^* ranging between 0.1 and 1 (i.e. for length scales of order $\mathcal{O}(d^*)$), the slope of the spectrum is approximately equal to −1.2, which suggests that the fluctuations of the bed profile at these scales are nearly random (i.e. the scales in this range are uniformly present). Consequently, in this range the spectrum of the bed slope, which is equal to $2\pi k^{*2} S_{\eta\eta}^*$, increases with increasing values of k^* and reaches a relative maximum at $k^*d^* \sim 0.5$. In other words, most of the fluctuations of the bed slope in such range of wave numbers are characterised by the length scale $2d^*$. Nikora et al. (1997) showed that such “bulges” of the bed profile spectra are associated with scale transitions, for instance between the meso- and micro-scales. Finally, for values of k^*d^* larger than 1 the spectrum decreases with slope −4.3, which was also observed by Kidanemariam and Uhlmann (2017). The latter range is not relevant for the characterization of the bedform geometry and the trend of the spectrum is possibly related to the shape of sediment particles.

Mazzuoli et al. (2016) showed that the interaction between a few spheres rolling over a plane bottom and the oscillatory flow, promoted the growth of certain disturbances and the decay of others, independently of the presence of roughness elements. Indeed, the formation of ripples is strictly related to the development of steady streaming. Presently, two-dimensional recirculating cells originated over the bed surface after a few oscillation

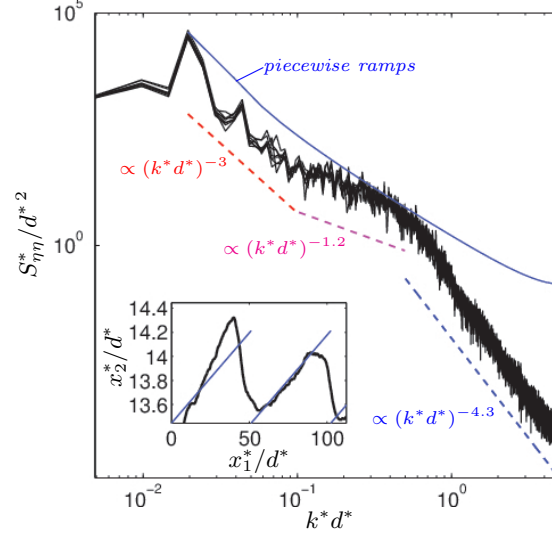


FIGURE 9: Spectra of the bed profile computed at the phases indicated in figure 8 for run 1. The solid (blue) line indicate the spectrum of the simplified configuration sketched in the small inset of the figure with periodic (blue) straight lines.

periods. In the final part of the simulations, the steady streaming appears as in figure 10 which was obtained by averaging the flow field in the spanwise direction and over the last 3 periods of run 1 and the last 5 periods of run 2. Let the intensity of the steady streaming, $\tilde{u}^*(t)$, be defined as the magnitude of the average in the interval $[t - T, t]$ and in the spanwise direction of the flow field, namely $\tilde{u}^* = \langle (\tilde{u}_1^{*2} + \tilde{u}_2^{*2})^{1/2} \rangle_{x_1 x_2}$, where $\tilde{u}_i^* \equiv \langle u_i \rangle_{T, x_3}^*$ is the i -th component of the period-and-spanwise averaged fluid velocity and $i = 1, 2$. Figure 11a shows that, in run 1, the value of \tilde{u}^*/U_0^* initially decreases, then starts to increase and attains an exponential growth from approximately the 10th oscillation period on, similarly to ripples of wavelength λ_η . Moreover, the evolution of dominant wavelength of the bed profile in figure 7a matches closely the evolution of $\lambda_{\tilde{u}_i}$, namely the dominant spatial periodicity of \tilde{u}_1 and \tilde{u}_2 in the vicinity of the bed, which is shown in figure 11b. Hence it is evident that the formation of ripples is coupled with the development of recirculating cells. The maximum velocity of the steady streaming is attained in the vicinity of the bed surface and is approximately equal to $1.5 \cdot 10^{-2} U_0^*$ and $0.6 \cdot 10^{-2} U_0^*$ for runs 1 and 2, respectively. Close to the bed, the spatial periodicity and the flow direction of recirculating cells promote the accretion of the ripples characterised by wavelength equal to λ_η . In particular, 4 pairs of recirculating cells can be observed for run 1 and 2 pairs for run 2. However, figure 10a, which refers to run 1, shows that recirculating cells with different periodicity superimpose above the bed and at $x_2 = 13$ only 2 pairs of recirculating cells can be detected. This is compatible with the evolution of the bed profile described above, in particular with the growth of the mode characterised by $k^*\delta^* = 0.24$, as shown in figure 6a. In run 2, contrarily, recirculating cells do not merge far from the bed (cf. figure 10b).

3.2 Dynamics of surficial particles

The process generating the ripples has been described as primarily being driven by the steady secondary flow arising in the boundary layer. In this section, we will evaluate

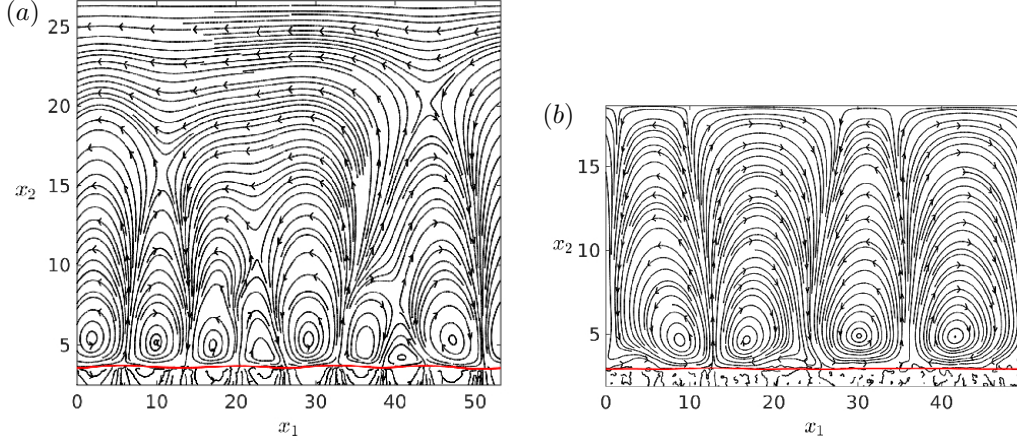


FIGURE 10: Steady streaming visualised by means of streamlines of the spanwise and time averaged flow field. The thick solid (red) lines indicates the average bed profile. Panels (a) and (b) refer to runs 1 and 2.

the role that moving particles play in the coupled problem of the bed surface evolution. Blondeaux (1990) found that the first observable (often called *critical*) wave number of ripples plotted versus Re_δ (for fixed values of the other parameters) exhibited discontinuities whenever particles in motion interacted with a different number of recirculating cells. Indeed, the selection of the critical wave number is closely related to the ratio between the *sediment semi-excursion*, ℓ_s^* , namely the amplitude of particle oscillations in the streamwise direction, and the wavelength of ripples, λ_η^* . However, ℓ_s^* is difficult to measure in the laboratory and Blondeaux (1990) replaced it in his study with the fluid semi-excursion, ℓ_f^* , since the two quantities are well correlated. Mazzuoli et al. (2016), who investigated by DNS the dynamics of a small number of spherical particles in an oscillatory boundary layer, computed the particle semi-excursion and found that it tended to increase almost linearly during the first oscillation periods, independently of the presence of bottom roughness, as long as particle-particle interactions were relatively unimportant (tests 2, 3 and 4 of Mazzuoli et al., 2016). The evolution of ℓ_s^* was more complex when many particles were considered. Presently, the motion of the *top-layer particles*, i.e. the spheres at the bed surface, is investigated. Top-layer particles consist of $\mathcal{O}(2 \cdot 10^4)$ spheres. Approximately 12% of these particles in run 1, and 15% in run 2, are crest particles, i.e. lay within a distance d^* from the sphere on top of the bed. The top-layer particles are tracked during each half-period starting from the phase, χ , when particle motion ceases and then restarts in the opposite direction.

In particular, the particles that at time $t_j^{(in)} = \pi(j + \chi)$, $j = 0, 1, 2, \dots$ are top-layer particles, are tracked for a half-period, χ being equal to 0.2 for both run 1 and run 2. Crest particles are more exposed to the flow, which gives them higher mobility than those lying in the troughs between the ripples. The trajectories of crest particles obtained for two periods of simulation 1 (when four ripples are present) are marked in figure 12. Figure 12 shows that, at the end of an oscillation, most of the particles recover almost the initial position except a few particles which can escape a ripple and reach the neighbouring one.

Figure 13a shows the probability that the semi-excursion, the time-maximum drag force and time-minimum drag force acting on the top-layer particles selected at the

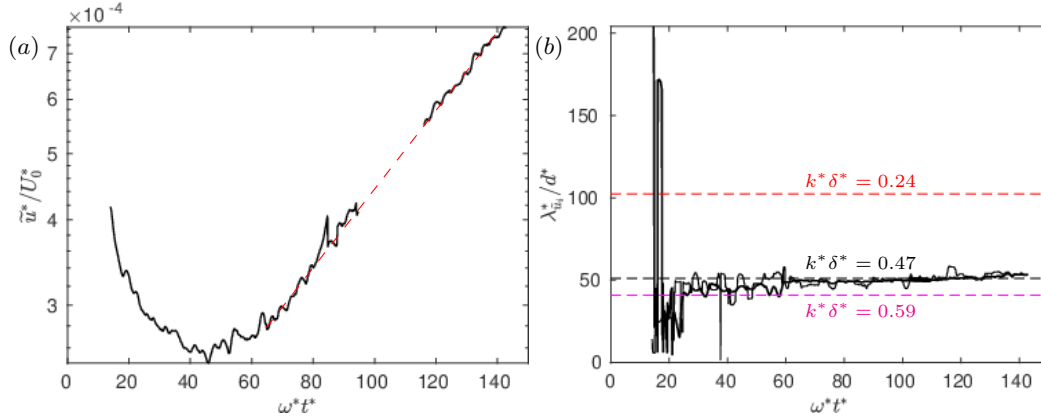


FIGURE 11: Panel (a) shows the magnitude of the steady streaming averaged over the x_1x_2 -plane, \tilde{u}^* , normalised by U_0^* and plotted versus time with the vertical axis in logarithmic scale. In panel (b) the dominant wavelength of the streamwise (thick line) and wall-normal (thin line) components ($i = 1, 2$) of the steady streaming velocity at $x_2^* = 3.90\delta^*$. Ripples appear nearly when the growth rate attains an exponential trend with constant rate. Each point of the curve is referred to the time-averaged value computed over the previous period for run 1.

instants $t_j^{(in)}$, $j = 36, 38, \dots, 41$, of run 1 and located within $[x_1 - D, x_1 + D]$, exceed the threshold values $0.5 \lambda_\eta^*$, $+0.1 F_{ref}^*$ and $-0.1 F_{ref}^*$, respectively, with $F_{ref}^* = \frac{1}{2} \rho^* U_0^* \omega^* \delta^{*3}$. Similarly, figure 13b refers to the interval between the $t_{54}^{(in)}$ and $t_{59}^{(in)}$, which is in the final part of simulation 2. For run 1, the values of the particle semi-excursion range between 0 and about $0.7 \lambda_\eta^*$. Figure 13a illustrates that the probability to observe large values of ℓ_s^* increases in the vicinity of the ripple crests while it is approximately halved in the troughs. In fact, the drag force acting on crest particles is significantly larger than the drag force acting on other particles, which causes crest particles to move longer (and farther) in the flow direction. Crest particles, at time $t = t_j^{(in)}$, are not aligned along the center line between the ripple troughs where the streamlines of recirculating cells converge (cf. figure 10), instead, as described in § 3.1, they are mostly piled on the side of each ripple opposite to the flow direction. Therefore, the probability curves related to the drag in figure 13a are asymmetric with respect to the center line of ripples. Another consequence of the asymmetric shape of ripple profile is that only a small amount of crest particles reach the neighbouring ripple during a half-period, although visualisations show that several crest particles display values of ℓ_s^* larger than $0.5 \lambda_\eta^*$, because at $t = t_j^{(in)}$ most of them are located farther than $0.5 \lambda_\eta^*$ from the downstream boundary between adjacent ripples. As a result, we observe the ripple crests moving to and fro over the span of λ_η^* . Similar dynamics can not be detected for run 2 by visual inspection of figure 13b. In this case, the variability of the drag force acting on top-layer particles is not as pronounced as in run 1 and, as shown in the following, results in the slower evolution of ripples. Also the semi-excursion of top-layer particles is almost independent of the streamwise coordinate and exhibits large values because the average (viscous) drag acts uniformly on the top-layer particles and is relatively strong. The drag coefficient for an isolated particle of run 2, i.e. the drag force normalized by the reference quantity $\frac{1}{2} \rho^* U_0^{*2} d^{*2}$, is approximately two times larger than in run 1). This is shown more clearly in section 3.3 where the sediment flux is related to the shear stress acting on the bed surface.

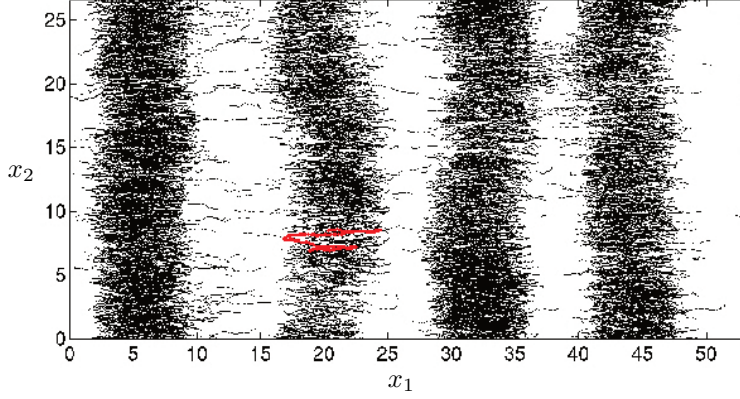


FIGURE 12: Trajectories of crest particles during the time interval $126.3 < t < 138.9$ (2 oscillation periods) of simulation 1. The trajectory of one particle is highlighted by a thick red line.

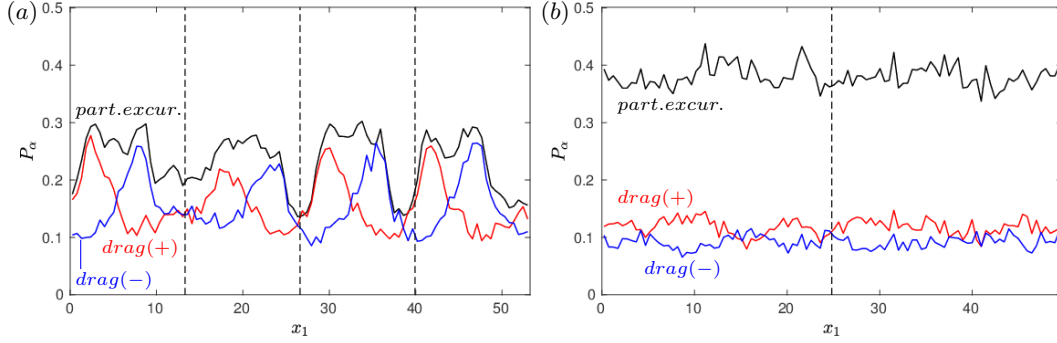


FIGURE 13: Probability that top-layer particles located at the instants $t = t^{(in)}$ (for the last 5 oscillation periods of each run) in a certain position x_1 experience semi-excursion $\alpha \equiv |\ell_s^*| > 0.5 \lambda_\eta^*$ (black lines) or time-maximum (over each half-period) drag force $\alpha \equiv \max_T \langle F_{1s}^* \rangle > +0.1 F_{ref}^*$ (red lines) or $\alpha \equiv \min_T \langle F_{1s}^* \rangle < -0.1 F_{ref}^*$ (blue lines). Dashed lines are equispaced by λ_η^*/δ^* . The reference drag is defined as $F_{ref}^* = \frac{1}{2} \varrho^* U_0^* \omega^* \delta^{*3}$. Probabilities are computed over the last periods of run 1 (panel(a)) and run 2 (panel(b)).

In order to understand why the formation of ripples in run 1 occurs significantly earlier than in run 2, three quantities are presently considered for each top-layer particle throughout the simulations: the particle semi-excursion, the particle velocity and the drag force. Results are first shown in the following for the last simulated half-period, where the differences between the motion of crest particles and of other top-layer particles are pronounced. The probability density function (pdf) of ℓ_s was computed for the top-layer particles of both run 1 and run 2, which shows that approximately 88% of top-layer particles set into motion stop within a distance equal to $4 d^*$ from their (previous) rest position (see figure 14a). Among these sluggish particles there are also crest particles that, however, predominately exhibit large mobility, in particular for run 1. In fact, the core of the pdfs of ℓ_s^* , normalised by λ_η^* , is found nearly coincident between run 1 and run 2 (d^* , δ^* and ℓ_f^* are found to not be relevant scales of the pdf core), while the tail of the curves, which is representative of the most mobile particles, deviates because crest particles behave differently in the two simulations and differently from the other top-layer

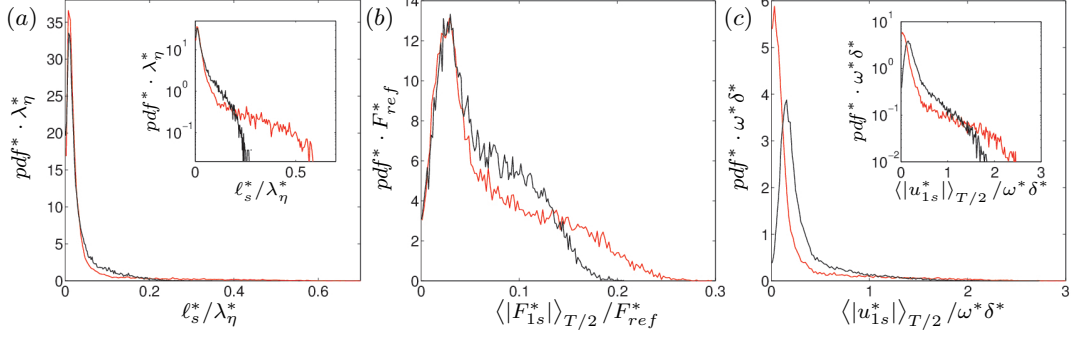


FIGURE 14: Probability density functions of particle semi-excursion (a), drag (b) and velocity (c) of *top-layer particles* for the 41st and 58th half-periods of run 1 (red lines) and run 2 (black lines), respectively. Drag force is normalised by $F_{ref}^* = \frac{1}{2} \varrho^* U_0^* \omega^* \delta^{*3}$. In the insets, the respective quantities are plotted in semi-logarithmic scale.

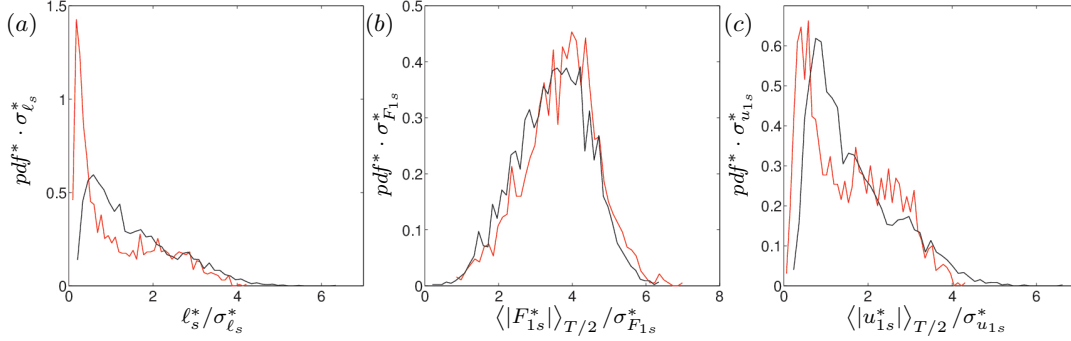


FIGURE 15: Probability density functions of particle semi-excursion (a), drag (b) and velocity (c) of *crest particles* for the 41st and 58th half-periods of run 1 (red lines) and run 2 (black lines), respectively. Drag force is normalised by $F_{ref}^* = \frac{1}{2} \varrho^* U_0^* \omega^* \delta^{*3}$. Quantities are normalised by the standard deviation of each sample.

particles. Such behaviour of crest particles reflects also on the particle velocity and drag, as can be understood from figures 14b,c. However, by restricting the sample to crest particles and scaling the quantities presently considered by their standard deviation, a fair matching of the pdfs can be obtained, as shown in figure 15. This strategy is not relevant for non-crest particles. The existence of two separated scales suggests that (at least) two types of particle motion coexist: a “regular motion” dominated by viscous forces (slow particles) and an “erratic motion” affected by particle-particle interactions that manifest themselves in random fluctuations of particle forces (crest particles): about 50% of crest particles of run 1 show a wide range of values of ℓ_s^* (between $0.10 \lambda_\eta^*$ and $0.45 \lambda_\eta^*$) with a nearly constant distribution of probability. Instead, the values of ℓ_s^* for run 2 are more accumulated around the mean value ($0.08 \lambda_\eta^*$) than in the other simulation. This is also emphasized by the ratio between the standard deviation, $\sigma_{\ell_s}^*$, and the mean value, $\langle \ell_s^* \rangle_s$, being equal to 0.88 and 0.67 for runs 1 and 2, respectively. The fact that λ_η^* is not a relevant scale for the semi-excursion of crest particles appears from the values of the statistics shown in table 4. The standard deviation $\sigma_{\ell_s}^*$ computed for run 2 appears significantly smaller than that of run 1 when normalised by λ_η^* . However, the value for each run is about 0.03 when normalised by ℓ_f^* , which is actually a relevant

scale for the semi-excursion of crest-particles. The values of $\langle \ell_s^* \rangle_s$ for crest particles are equal to $3.6 \cdot 10^{-2} \ell_f^*$ and $5.7 \cdot 10^{-2} \ell_f^*$ for runs 1 and 2, respectively, which are smaller but of the same order (approximately half) of the value obtained by Mazzuoli et al. (2016) at the end of test nr. 6. Actually, in the present case there are factors that contribute to increase the friction between sediments, among them the bed surface is not macroscopically flat as in the cases investigated by Mazzuoli et al. (2016) and the number of moving particles (and, consequently, of collisions) is much larger. The maximum value of particle excursion, $\max_s \ell_s^*$, for run 1 is approximately equal to $0.15 \ell_f^*$ and is comparable with those computed from one of the experiments of Rousseaux et al. (2004) ($Re_\delta \simeq Re_d = 135$, $s = 2.5$) which fell in the range $[0.15, 0.25] \ell_f^*$.

run	$\frac{\lambda_\eta^*}{\ell_f^*}$	$\frac{\langle \ell_s^* \rangle_s}{\lambda_\eta^*}$	$\frac{\langle F_{1s}^* \rangle_{T/2,s}}{F_{ref}^*}$	$\frac{\langle u_{1s}^* \rangle_{T/2,s}}{\omega^* \delta^*}$	$\frac{\sigma_{\ell_s}^*}{\lambda_\eta^*}$	$\frac{\sigma_{F_{1s}}^*}{F_{ref}^*}$	$\frac{\sigma_{u_{1s}}^*}{\omega^* \delta^*}$
1	0.208	0.173	0.156	0.953	0.152	0.042	0.626
2	0.693	0.082	0.111	0.677	0.055	0.032	0.410

TABLE 4: Statistics of crest particles.

The discrepancies between the pdfs of the two simulations are not strictly associated with the presence of ripples, as one could be tempted to presume, because the same differences were present since the initial wave cycles when bedforms were not yet developed. Instead, they can be attributed to the different values of the Keulegan-Carpenter number, K_c . In fact, large values of ℓ_s are associated with large values of ℓ_f . Moreover, the contribution to the average drag force acting on the particles due to the presence of recirculation cells is smaller in run 2 than in run 1 which leads to more homogeneous distribution of drag over the bed surface. Note that most frequently (in the sense of probability) top-layer particles exhibit a creeping velocity, in particular in the case of run 1 which shows a wider gap between very slow and fast moving particles than run 2 (cf. figure 14c). Analogous to the process of segregation for poly-dispersed particulate flows, which occurs because of particle inertia when sediment particles differ in size and/or density, here the growth of bed surface perturbations is promoted by the non-uniform distribution of drag over top-layer particles (due to the steady streaming) and is faster if the non-homogeneity is more pronounced.

In principle, the mechanism at the origin of the patterns of spheres on the surface of a movable bed is similar to that observed by Mazzuoli et al. (2016) for beads rolling on a rough plane bottom (tests 4 and 6). In test no. 6 of Mazzuoli et al. (2016), several movable beads were initially aligned in the direction of flow oscillations and rapidly spread laterally until, in a few oscillations, they were randomly scattered over the whole bottom. The latter is approximately the initial configuration of the present simulations. The evolution of the values of ℓ_s , F_{1s} and u_{1s} , averaged over top-layer or crest particles and over each half-cycle, are shown in figure 16. The values of the considered quantities for top-layer particles are approximately constant throughout simulation 2, except a short initial transient, while a slight monotonic decrease of the three quantities can be noted relative to crest particles. During the transient, both the semi-excursion and the velocity of top-layer particles decrease because the spheres attain a closely packed configuration. Conversely, crest particles of run 1 manifest increasing mobility since the beginning of the simulation and show an approximately linear growth of the average ℓ_s and u_{1s} , while drag seems to asymptotically reach a constant value after the initial transient. The increase of mobility of crest particles is due to the emergence of ripples which push crest particles

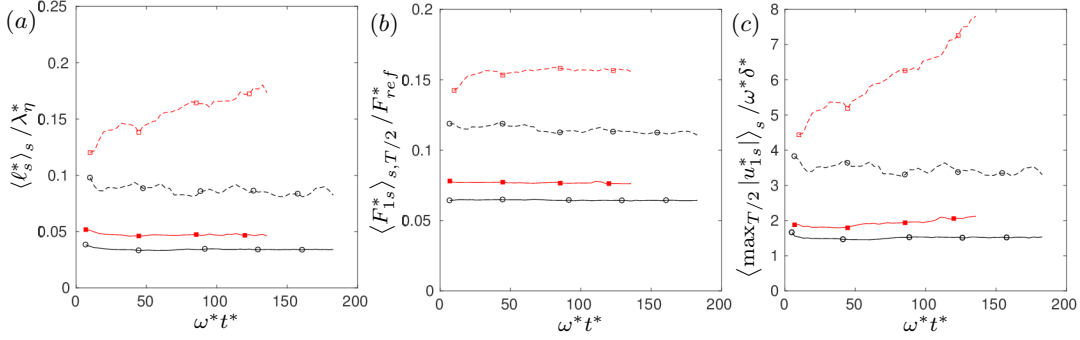


FIGURE 16: Statistics of the motion of top-layer (solid lines) and crest (dashed lines) particles: (a) mean particle semi-excursion, (b) maximum velocity, (c) mean time-maximum drag. The values are computed for each half-period of simulation 1 (red lines/squares) and simulation 2 (black lines/circles). Particle semi-excursion for run 1 increases approximately with a linear trend: similar trend was observed by Mazzuoli et al. (2016) in their tests no. 2,3,4.

towards regions of the boundary layer characterized by higher velocity. The effect of the exponential growth of the ripple amplitudes is partly opposed by that of increasing inter-particle collisions. Since the inertia of particles is relatively small in both runs 1 and 2 (as indicated by the large values of K_c), the drag force reaches a limit as it balances the bed friction. Thus, the relative particle velocity, on which the viscous drag depends, remains constant while the particle absolute velocity. In fact, as will be clarified in the following section, the viscous drag dominates the other force contributions in the phases when the bed shear stress is at a maximum.

3.3 Bed shear stress, incipient particle motion and sediment flow rate

The wall-normal dependent total shear stress is a sum of the fluid shear stress τ_f^* and the contribution stemming from the fluid-particle interaction τ_p^* , viz.

$$\tau_{tot}^* = \tau_f^* + \tau_p^* \quad (12)$$

where the fluid shear stress (under a turbulent flow condition) is comprised of the viscous and Reynolds shear stress contributions:

$$\tau_f^*(x_2^*) = \varrho^* \nu^* \frac{\partial \langle u_1^* \rangle}{\partial x_2^*}(x_2^*) - \varrho^* \langle u_1^* u_2^* \rangle(x_2^*), \quad (13)$$

where the dependence on t^* is omitted for the sake of clarity. While x_3 is a homogeneous direction for the total shear stress also in the presence of ripples, relatively small fluctuations about τ_{tot}^* can be observed in the streamwise direction when the rolling-grain ripples form. Thus, τ_{tot}^* is the average total shear stress acting on the bed. It is expected that, in the present configuration, the Reynolds shear stress has negligible contribution as the flow is essentially laminar. In the context of the immersed boundary method, the stress exerted by the particles is given by

$$\tau_p^*(x_2^*) = \varrho^* \int_{x_2^*}^{L_{x_2}^*} \langle f_1^* \rangle dx_2^* \quad (14)$$

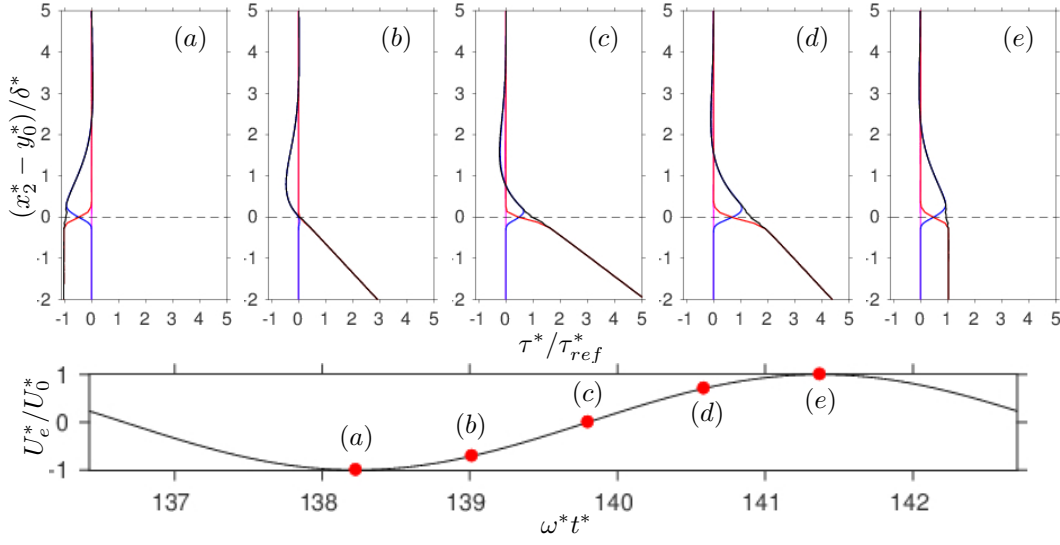


FIGURE 17: Sample wall-normal profile of the fluid viscous shear stress (blue line), Reynolds shear stress (magenta line), stress stemming from the fluid-particle interaction (red line) as well as the total shear stress τ_{tot} (black line). The profiles correspond to selected times which are indicated in bottom panel. Data corresponds to run 1.

where f_1^* is the streamwise component of the immersed boundary method volume forcing exerted on the fluid, transferred to the Eulerian grid (cf. §2). In a stationary channel flow scenario, the total shear stress varies linearly in the wall-normal direction with a slope equal to the value of the imposed driving pressure gradient. In the present OBL configuration however, as a result of the non-stationarity, τ_{tot}^* responds to the pressure gradient in a complex non-linear behavior. Figure 17 shows sample wall-normal profiles of the different contributions to the total shear stress, non-dimensionalised by $\tau_{ref}^* = \frac{1}{2}\varrho^*U_0^*\omega^*\delta^*$, at different time instants. As is expected, the contribution from the Reynolds shear stress is negligibly small across the entire wall-normal interval which is a further indication that the flow has not separated behind the ripple crests. In the clear fluid region, that is, in the region which is essentially devoid of sediment particles, only the fluid viscous shear stress contributes to τ_{tot} . On the other hand, deep inside the sediment bed sufficiently below the fluid-bed interface, τ_f vanishes and τ_{tot} entirely is comprised of the stress exerted by the sediment particles. It is worth noting that, in this region, τ_{tot} exhibits a linear variation with a slope equal to the imposed pressure gradient. This means that the particle shear resistance, which is proportional to the submerged weight of sediment bed, is instantaneously in equilibrium with the oscillating driving force (neglecting the small particle velocities in this region). In between these two regions, there exists a third “active layer” region, hereafter referred to as *mobile layer*, where both τ_f and τ_p contribute to the total shear stress and where the particle erosion-deposition processes take place. Although there is no clear demarcation of these regions, it is observed that the thickness of the mobile layer varies depending on different phases of the oscillation period.

For modeling purposes, it is common practice to relate the non-dimensional boundary

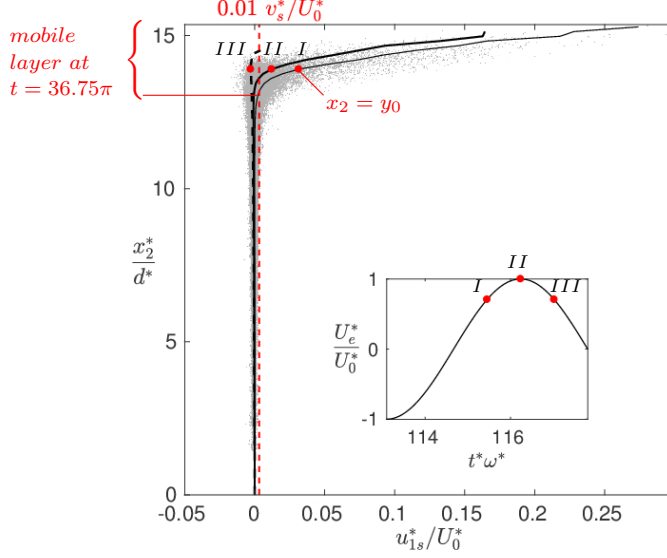


FIGURE 18: In the main panel, the streamwise component of the particle velocity is plotted as a function of the wall-normal coordinate of run 1. Shaded by grey dots are the velocity of each particle at the instants $t = 36.75\pi$ (I), $t = 37.00\pi$ (II) and $t = 37.25\pi$ (III) (phases are indicated in the small inset), while thin solid, thick solid and dashed lines indicate the respective (binned) average values.

shear stress $\tau_b^* = \tau_{tot}^*(x_2^* = y_0^*)$, i.e. the Shields number

$$\theta = \frac{\tau_b^*}{(\varrho_s^* - \varrho^*)g^*d^*} \quad (15)$$

to the sediment flow rate. The value of y_0^* is chosen as the distance from the bottom at which the average particle volume fraction $\langle \phi_s \rangle$ reaches 0.1. The instantaneous volumetric flow rate of the particle phase (per unit span), q_s^* , is given by

$$q_s^*(t^*) = \frac{\pi d^{*3}}{6 L_{x_1}^* L_{x_3}^*} \sum_{l=1}^{N_p} u_{1s}^{*(l)}(t^*), \quad (16)$$

where $u_{1s}^{*(l)}(t^*)$ is the streamwise component of the velocity of the l -th mobile particle at time t^* . Since spherical particles do not gear to each other and can slide more easily than sand grains, many particles experience non-zero velocities, even if they are located below the bed surface. Thus, in order to exclude all particles which do not contribute to the shear induced particle flux, a streamwise velocity threshold is set at 1% of the gravitational velocity of particles, v_s^* (similar results are obtained even considering the threshold at a small percentage of $\omega^*\delta^*$). The particle selected with such criterion approximately coincide with those constituting the mobile layer (cf. figure 18).

Figure 19 shows the absolute value of the particle flow rate, normalised by $d^*v_s^*$, as a function of the absolute value of the Shields number for the last four periods of run 1 and run 2. The arrows indicate the time-development along the loop swept in a half-period. Following the loop, the particle flow rate exhibits a minimum in the early deceleration phase. Then, while the free-stream velocity is still decelerating and the Shields number

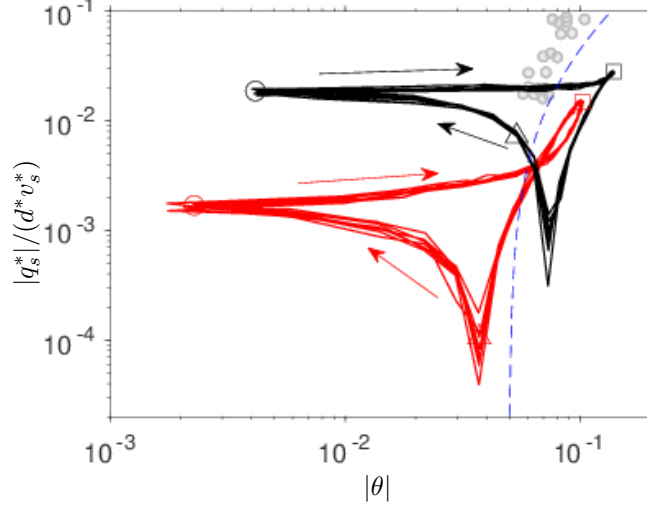


FIGURE 19: Instantaneous dimensionless particle flow rate, normalized by the inertial scaling $d^* v_s^*$, as a function of the Shields number θ during the last four cycles of the simulation interval. Run 1 (red line); run 2 (black line). The dashed-line represents the the Meyer-Peter & Müller formula (Wong and Parker, 2006) for steady turbulent flow conditions $q_s = 4.93(\theta - \theta_c)^{1.6}$. The symbols \triangle , \circ , \square indicate phases $t = 9/8\pi$, $t = 41/32\pi$ and $t = 7/4\pi$. Gray circles indicate the experimental observations of Gilbert and Meyer-Peter (Nielsen, 1992).

decreasing, the particle flow rate increases under the action of the imposed driving pressure gradient. Subsequently, the next acceleration phase starts and the Shields number rises. Finally, approximately at the phase $\frac{3}{4}\pi$ (i.e. $\pi/4$ after the flow reversal), both the Shields number (i.e. the boundary shear stress) and the sediment flow rate are maximum. It can be noted that, except for two or three instants, each value of $|\theta|$ correspond to two values of the dimensionless sediment flow rate. It is therefore clear, by comparing the diagrams of figure 19 obtained for the present runs with the experimental measurements of Gilbert and Meyer-Peter (grey symbols, Nielsen, 1992) and with the Meyer-Peter & Müller formula (dashed line, Wong and Parker, 2006) obtained for stationary channel flows, that the effects of the flow unsteadiness reflect strongly on the motion of particles and should be taken into account in the models of sediment transport. Indeed, during the flow reversal, which is characterised by large values of the forcing pressure gradient and relatively small values of the bed shear stress, the sediment flow rate is not negligible. Hence, coarse prediction errors could be avoided by relating the sediment flow rate to a combination of the Shields number and some dimensionless expression of the pressure gradient such as the instantaneous Sleath parameter (Foster et al., 2006; Frank et al., 2015), defined as:

$$\mathcal{S} = -\frac{d^*}{\varrho^* v_s^{*2}} \frac{dp_f^*}{dx_1^*} = \frac{\psi}{K_c} \sin(t) , \quad (17)$$

where the expression (3) was substituted in the second equality. Since the values of the Keulegan-Carpenter number, K_c , are large in both the present simulations, the contribution of the viscous drag is expected to dominate over that induced on the spheres by the pressure gradient. Besides the direct contribution on the particle force, the pressure gradient also causes the acceleration of the interstitial fluid which, due to its small inertia, responds much earlier than the clear fluid above the bed. Thus, such viscous pore

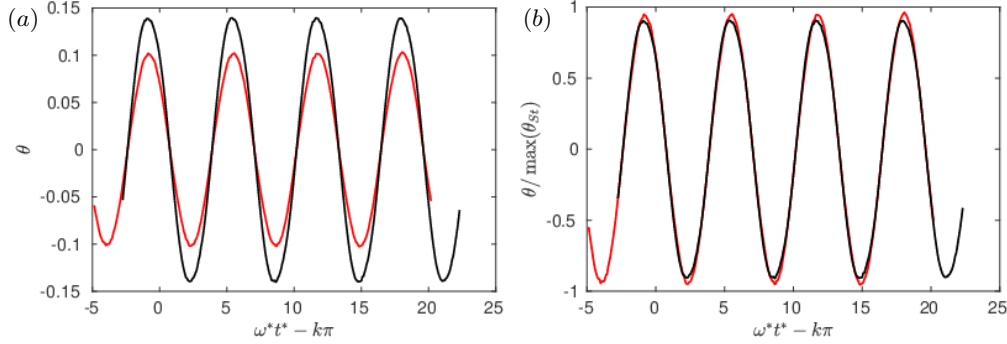


FIGURE 20: Evolution of the Shields number for run 1 (red line) and run 2 (black line) during the last simulated periods. In panel (b) the Shields number is normalized by the maximum Shields number attained in the absence of particles, i.e. in a Stokes boundary layer.

flow develops and can mobilize the sediment particles much earlier than the bed shear stress becomes appreciable. Even though the velocity of the particles set into motion during the flow reversal is small, the thickness of the mobile layer is relatively large in these phases because the pressure gradient acts uniformly on the entire bed. Finally, as the values of $|\theta|$ become large, crest particles, which are more exposed to the flow in the boundary layer and exhibit values of streamwise (particle) velocity of order $\mathcal{O}(0.1) U_0^*$, mostly contribute to the sediment flow rate.

Figure 19 also shows that, at corresponding phases, the Shields number and, therefore, the sediment flow rate normalised by $d^* v_s^*$, are larger in run 2 than in run 1. To understand such difference it is useful to compare the Shields number to that we would observe in absence of sediments, i.e. in a Stokes boundary layer:

$$\theta_{(St)} = \frac{\psi}{Re_\delta} [\sin(\omega^* t^*) - \cos(\omega^* t^*)] . \quad (18)$$

Figure ?? shows that, scaling the Shields number by the maximum value of $\theta_{(St)}$, the resulting curves of runs 1 and 2 almost overlap and the amplitude of oscillations is nearly equal to unity, because the bed shear stress approaches that of a Stokes boundary layer in both runs. Consequently, the quantity $\frac{1}{2} \varrho^* U_0^* \omega^* \delta^*$ is a relevant scale for the bed shear stress. Hence, for a given value of ψ , by increasing the value of Re_δ^* the Shields parameter decreases (like in the present case) until turbulence appears and further modes of sediment transport occur (e.g. saltation). Moreover, it can be noted that the maximum value $\max(\theta_{(St)}) = \sqrt{2} \frac{\psi}{Re_\delta}$ equals the maximum value of the Sleath number, i.e. approximately the maximum effect of the imposed pressure gradient on an isolated particle, $\max(\mathcal{S}) = \frac{\psi}{K_c} = 2 \frac{d^*}{\delta^*} \frac{\psi}{Re_\delta}$, if $d^*/\delta^* \sim 0.7$. Therefore, even though the maximum shear stress and the maximum imposed pressure gradient are reached at different phases of the oscillation period, in the present cases (and in most of the experiments made by [Blondeaux et al., 1988](#)) viscous effects prevail. It can be useful to point out that typically, in the field, the ratio d^*/δ^* does not significantly vary with respect to the other parameters (e.g. for $0.2 \text{ mm} < d^* < 1 \text{ mm}$ and $T \sim 10 \text{ s}$, $0.1 < d^*/\delta^* < 0.6$), thus the ratio $\frac{\psi}{Re_\delta}$ can be practically used as the only parameter driving the sediment flow rate (as long as the flow is not turbulent). It can be inferred from the present results that the growth rate of ripples is related to the maximum sediment flow rate. In particular, the growth rate of ripples increases if the maximum bed shear stress is not much larger than

the critical value of incipient sediment motion, sediments being more sensitive to the effect of the steady streaming. Consequently, if the ratio $\frac{\psi}{Re_\delta}$ is close to $\theta_{cr}/\sqrt{2} \sim 0.035$ ripples form more rapidly. In fact, for runs 1 and 2, $\frac{\psi}{Re_\delta}$ is equal to 0.076 and 0.110, respectively, and ripples form much more slowly in case 2. The relevance of $\frac{\psi}{Re_\delta}$ for the prediction of ripple genesis was also emphasized by Blondeaux (1990) (see figure 11) because it is related to the ratio $\frac{\langle \ell_s^* \rangle_s}{\lambda_\eta^*}$. In particular, the dimensionless parameter used by Blondeaux (1990) and by other authors before was $\frac{d^*}{(s-1)g^*T^{*2}}$ which is equal to $\frac{1}{\pi^2} \frac{\psi}{Re_\delta^2} \frac{d^{*2}}{\delta^{*2}}$ and was empirically found controlling the ripple wavelength.

4 Conclusions

The origin and development of ripples in an oscillatory flow was investigated by means of direct numerical simulations. Two experiments were reproduced which were carried out by using medium sand at moderate values of the Reynolds number. The experiments significantly differed in the frequency and amplitude of the free-stream velocity oscillations (i.e. both in the Stokes and particle Reynolds numbers, Re_δ and Re_d). After approximately ten oscillations, two-dimensional patterns arose which then coarsened turning into rolling-grain ripples. The wavelengths characterizing the ripples in the simulations, in the limits set by the domain size, are comparable with those observed in the experiments and with the predictions obtained by linear stability analysis. The bed surface is identified for each discrete instant. The Fourier analysis of the bed profile shows that, after an initial transient where patterns form then merge or disappear, a few wave numbers grow in amplitude and finally one wave number becomes dominant. Ripples form clearly in one of the two simulations (run 1) while two-dimensional patterns are observed in the second simulation (run 2), since the dynamics of the bed are somewhat slower in the latter case. In run 1 the growth of the bed-surface fluctuation amplitude normalised by the particle diameter is found to follow an exponential trend with exponent equal to $1.46 \cdot 10^{-2} \omega^* t^*$. The secondary flow arising from the flow instability consists of steady recirculating cells which are responsible for the formation of ripples, since they tend to pile up the sediment particles at the nodes where streamlines converge and to scour where streamlines diverge close to the bed surface. The evolution of ripples and the development of recirculating cells are strictly related. Ripples of run 1 exhibit an asymmetric shape for most of the oscillation period, with the lee side steeper than the stoss side, except in the phases characterised by the largest bed shear stress when the ripple crests migrates in the direction of the mean flow.

The sediment particles at the flow-bed interface (top-layer particles) are tracked during the wave cycles and the velocity and the drag force are computed. Two distinct kinds of particle motion are identified: most of the top-layer particles, in particular those lying in the troughs of ripples, roll for $\mathcal{O}(1) d^*$ in the flow direction then they stop. The excursion of these particles, i.e. the displacement in the streamwise direction that they experience for each half cycle, is found to scale with the wavelength of ripples for the present simulations. Similarly, the drag force and, more weakly, the velocity of these “slow” particles scale with reference quantities obtained as combinations of ω^* , U_0^* and δ^* . However, the sediment particles lying on the crest of ripples (crest particles) are subjected to stronger drag force which causes large excursions in some cases of $\mathcal{O}(0.1) \ell_f^*$, i.e. comparable with the fluid excursion far from the bed. Therefore, such particles are provided with larger momentum than others. These “fast” particles, though they do not saltate, encounter several collisions with other particles that contribute to increase the

variance of quantities associated with their motion. It is found for the present cases that the wider the difference of motion between “slow” and “fast” particles, the more rapid the growth of bedforms is. In this sense the origin of ripples can be seen in analogy with the phenomenon of segregation of sediments of different size or density, since in both cases a non-uniform distribution of momentum is transferred from the flow to the sediments, in one case because of the non-uniform distribution of the mass of sediment grains, while in the present case because of the non-uniform distribution of the velocity field (due to the presence of the recirculation cells).

Finally, the sediment flow rate is computed and compared with global quantities characterising the fluid-sediment interaction. The Shields number and the dimensionless (external) pressure gradient are considered. A fair correlation between the sediment flow rate and the Shields number is found in the phases of the oscillation period when the bed shear stress reaches the maximum value. In such phases the predictions obtained by means of the Meyer-Peter & Müller formula, i.e. based on steady flow regime and uniquely on the value of the Shields number, are approached. However, in the phases of the oscillation period characterised by small values of the bed shear stress and large values of the (external) pressure gradient, a significant sediment flow rate was observed which cannot be explained on the basis of the instantaneous Shields number, which is actually vanishing. Thus, the Shields number should be combined with the dimensionless pressure gradient to improve the accuracy of prediction of the sediment flow rate. In conclusion, for the purpose of modelling the formation of bedforms under sea waves, the effect of the unsteadiness on the transport of sediments is remarkable in the absence of turbulent events as in the present cases. For the range of values of d^*/δ^* that typically characterise a sandy seafloor, the parameter ψ/Re_δ controls the growth rate of ripples. In particular, the closer ψ/Re_δ is to $\theta_{cr}/\sqrt{2}$, the more rapid the formation of ripples results.

An extension of the present investigation aimed at exploring the regions of the parameter space characterised by the turbulent flow regime would be of immense help for the development of reliable sediment transport models and for the estimation of the bed evolution. Considering the high computational cost and the formidable simulation time required by the present simulations, which exceeded the 10 million CPU hours and approximately 1 million time steps (i.e. running for ~ 480 days on 64 “Ivy Bridge” computing nodes), the direct numerical simulation of the formation of bedforms in a turbulent oscillatory flow is not yet feasible as it would require much larger domain and finer spatial and temporal resolutions than the present ones. Nonetheless, fundamental insights on the mechanics of sediment transport in a turbulent oscillatory boundary layer could be obtained by reducing the size of the computational domain to that required by turbulence to develop, namely to the minimal flow unit.

This study has been funded by the Office of Naval Research (U.S., under the research project no. 1000006450 - award no. N62909-17-1-2144) and by the Deutsche Forschungsgemeinschaft (Germany, project UH 242/4-2). We acknowledge the generous support from CINECA (Bologna, Italy) for the computational resources provided on FERMI under grant TEST SEA (PRACE 7th-call) and from the Steinbuch Center for Computing (KIT, Karlsruhe) for the resources provided on ForHLR I under the grant DNSBEST-SEA. The Authors wish to thank Paolo Blondeaux and Giovanna Vittori for the fruitful discussions in particular concerning the interpretation of the bed evolution and the description of the experiments they carried out in Cambridge in 1988. The numerical investigations were performed during the time the second author (AGK) was employed by the Institute for Hydromechanics, Karlsruhe Institute of Technology (KIT).

References

- Aussillous, P., Chauchat, J., Pailha, M., Médale, M., Guazzelli, É., 2013. Investigation of the mobile granular layer in bedload transport by laminar shearing flows. *Journal of Fluid Mechanics* 736, 594–615.
- Blondeaux, P., 1990. Sand ripples under sea waves part 1. ripple formation. *Journal of Fluid Mechanics* 218, 1–17.
- Blondeaux, P., Sleath, J., Vittori, G., 1988. Experimental data on sand ripples in an oscillatory flow, rep. 01/88 inst. Hydraulics University of Genoa.
- Coleman, S., Nikora, V., 2011. Fluvial dunes: initiation, characterization, flow structure. *Earth Surface Processes and Landforms* 36 (1), 39–57.
- Davies, A., Ribberink, J., Temperville, A., Zyserman, J., 1997. Comparisons between sediment transport models and observations made in wave and current flows above plane beds. *Coastal Engineering* 31 (1-4), 163 – 198.
- Foster, D., Bowen, A., Holman, R. A., Natto, P., 2006. Field evidence of pressure gradient induced incipient motion. *Journal of Geophysical Research: Oceans* 111 (C5).
- Frank, D., Foster, D., Sou, I. M., Calantoni, J., Chou, P., 2015. Lagrangian measurements of incipient motion in oscillatory flows. *Journal of Geophysical Research: Oceans* 120 (1), 244–256.
- Hino, M., 1968. Equilibrium-range spectra of sand waves formed by flowing water. *Journal of Fluid Mechanics* 34 (3), 565–573.
- Hwang, K., Hwung, H., Huang, P., 2008. Particle motions on a plane floor under waves. 8th Int. Conf. Hydrodynamics, ICHD2008, 30 Sept.-3 Oct. 2008, Nantes, France, pp. 211–218.
- Jain, S. C., Kennedy, J. F., 1974. The spectral evolution of sedimentary bed forms. *Journal of Fluid Mechanics* 63 (2), 301–314.
- Kidanemariam, A. G., Uhlmann, M., 2014a. Direct numerical simulation of pattern formation in subaqueous sediment. *Journal of Fluid Mechanics* 750, R2.
- Kidanemariam, A. G., Uhlmann, M., 2014b. Interface-resolved direct numerical simulation of the erosion of a sediment bed sheared by laminar channel flow. *International Journal of Multiphase Flow* 67, 174–188.
- Kidanemariam, A. G., Uhlmann, M., 2017. Formation of sediment patterns in channel flow: minimal unstable systems and their temporal evolution. *Journal of Fluid Mechanics* 818, 716–743.
- Lyne, W., 1971. Unsteady viscous flow over a wavy wall. *Journal of Fluid Mechanics* 50 (01), 33–48.
- Mazzuoli, M., Blondeaux, P., Simeonov, J., Calantoni, J., 2017. Direct numerical simulation of oscillatory flow over a wavy, rough, and permeable bottom. *Journal of Geophysical Research: Oceans*.

- Mazzuoli, M., Kidanemariam, A. G., Blondeaux, P., Vittori, G., Uhlmann, M., 2016. On the formation of sediment chains in an oscillatory boundary layer. *Journal of Fluid Mechanics* 789, 461–480.
- Mazzuoli, M., Uhlmann, M., 2017. Direct numerical simulation of open-channel flow over a fully rough wall at moderate relative submergence. *Journal of Fluid Mechanics* 824, 722–765.
- Moon, S. J., Swift, J., Swinney, H. L., 2004. Role of friction in pattern formation in oscillated granular layers. *Physical Review E* 69 (3), 031301.
- Nielsen, P., 1992. Coastal bottom boundary layers and sediment transport. World scientific.
- Nikora, V. I., Sukhodolov, A. N., Rowinski, P. M., 1997. Statistical sand wave dynamics in one-directional water flows. *Journal of Fluid Mechanics* 351, 17–39.
- Pedocchi, F., García, M. H., 2009. Ripple morphology under oscillatory flow: 2. experiments. *Journal of Geophysical Research: Oceans* 114 (C12).
- Rousseaux, G., Stegner, A., Wesfreid, J. E., 2004. Wavelength selection of rolling-grain ripples in the laboratory. *Physical Review E* 69 (3), 031307.
- Scandura, P., Vittori, G., Blondeaux, P., 2000. Three-dimensional oscillatory flow over steep ripples. *Journal of Fluid Mechanics* 412, 355–378.
- Sleath, J., 1976. On rolling-grain ripples. *Journal of Hydraulic Research* 14 (1), 69–81.
- Sleath, J. F., 1984. Sea bed mechanics. John Wiley and Sons Inc., New York, NY.
- Stegner, A., Wesfreid, J. E., 1999. Dynamical evolution of sand ripples under water. *Physical review E* 60 (4), R3487.
- Thibodeaux, L. J., Boyle, J. D., 1987. Bedform-generated convective transport in bottom sediment. *Nature* 325 (6102), 341–343.
- Uhlmann, M., 2005. An immersed boundary method with direct forcing for the simulation of particulate flows. *Journal of Computational Physics* 209 (2), 448 – 476.
- Uhlmann, M., Chouippe, A., 2017. Clustering and preferential concentration of finite-size particles in forced homogeneous-isotropic turbulence. *J. Fluid Mech.* 812, 991–1023.
- Vittori, G., Blondeaux, P., 1990. Sand ripples under sea waves part 2. finite-amplitude development. *Journal of Fluid Mechanics* 218, 19–39.
- Vittori, G., Blondeaux, P., 1992. Sand ripples under sea waves part 3. brick-pattern ripple formation. *Journal of Fluid Mechanics* 239, 23–45.
- Wong, M., Parker, G., 2006. Reanalysis and correction of bed-load relation of meyer-peter and müller using their own database. *Journal of Hydraulic Engineering* 132 (11), 1159–1168.